Catena 220 (2023) 106699

Contents lists available at ScienceDirect

Catena

journal homepage: www.elsevier.com/locate/catena

Spatial variation in specific sediment yield along the Peruvian western Andes

Miluska A. Rosas [a,b,*], Willem Viveen [b], Veerle Vanacker [a,*]

[a] Earth and Life Institute, Georges Lemaître Centre for Earth and Climate Research, Université catholique de Louvain, Place Louis Pasteur 3, L4.03.08, 1348 Louvain la Neuve, Belgium
[b] Grupo de Investigación en Geología Sedimentaria, Especialidad de Ingeniería Geológica, Departamento de Ingeniería, Pontificia Universidad Católica del Perú, Av. Universitaria 1801, San Miguel, Lima, Perú

ARTICLE INFO

Keywords:
Suspended sediment concentration
Erosion
Topography
Climate
Land cover
Andes

ABSTRACT

The tropical Andes has been less studied in terms of erosion processes in comparison to other major mountain ranges in the world. Environmental gradients are steepest along the western flank of the Andes that is characterized by marked differences in vegetation, rough topography with deeply incised canyons, and highly variable and extreme precipitation patterns. Previous efforts mostly focused on sediment fluxes in large rivers draining to e.g. the Amazon basin while small to medium-sized rivers such as the ones flowing towards the Pacific Ocean have been relegated. They highlighted the link between sediment yield, anthropogenic and natural factors, e.g. climate, topography, river runoff, lithology and vegetation cover.

In this study, we identified the spatial patterns of specific sediment yield along the western slopes of the Peruvian Andes between 3° and 13° S latitude for 21 catchments. We collected and analysed data from 22 environmental factors to elucidate their importance on spatially varying sediment yield. The sediment load was derived from gauging stations, reservoir sedimentation and water turbidity over a 30-yr period. The specific sediment yield varies strongly along the Peruvian western Andes as a consequence of the spatial variation in climate, topography and land cover controlling sediment production and transport. We reported higher-than-average specific sediment yields for the central part (6°-11°S) with values of 2130 and 2300 t km^{-2} yr^{-1} and low and uniform yields of 39 to 551 t km^{-2} yr^{-1} in the southern part (11° − 14.5° S). Given the scarcity of data on sediment yield, we included an uncertainty assessment based on bootstrapping approaches as to get a better grasp on the potential range of specific sediment yields in the study region. Using statistical techniques including Spearman correlation rank, univariate and multivariate regression analyses, we were able to determine the importance of the 22 environmental variables on the specific sediment yield. About 55 % of the observed variance can be explained by river discharge (Q_{90}) and river steepness index (ks_{50}). By adding an anthropogenic variable based on land cover, the explained variance in SSY increases up to 63 %, however, the effects of land cover on specific sediment yield are not clear because of spurious correlation between land cover, river discharge and topography. Our study therefore provides important new insights in the ongoing scientific debate on sediment yield variability in the western Andes.

1. Introduction

Tropical (23°27′ N – 23°27′ S) mountain regions are susceptible to soil erosion due to steep topography, prevalent precipitation either seasonally or year-round, and a high probability of earthquakes and landslides (Aalto et al., 2006; Syvitski et al., 2014). A past study, based on global sediment delivery models, predicted that the modern sediment load in the tropics is 30 % higher than the pre-industrial load, and that the sediment delivery to the Pacific Ocean has increased by almost 10 % (Syvitski et al., 2005). Moreover, the area is prone to rapid land use change including deforestation (Hansen et al., 2013) and extreme precipitation events (Syvitski et al., 2014) that potentially induce an increase in sediment fluxes (Restrepo et al., 2009; Milliman & Farnsworth, 2011). A global assessment on soil erosion listed several tropical regions

---

* Corresponding author at: Earth and Life Institute, Georges Lemaître Centre for Earth and Climate Research, Université catholique de Louvain, Place Louis Pasteur 3, L4.03.08, 1348 Louvain la Neuve, Belgium.

E-mail addresses: miluska.rosas@pucp.pe, miluska.rosas@uclouvain.be (M.A. Rosas), veerle.vanacker@uclouvain.be (V. Vanacker).

https://doi.org/10.1016/j.catena.2022.106699
Received 1 March 2022; Received in revised form 27 July 2022; Accepted 6 October 2022

as Brazil, African territories along the Equator, India, Central Eastern Ethiopia, Mexico, Indonesia, and Peru as hotspots of erosion with erosion rates above 2 000 t km^{-2} yr^{-1} (Borrelli et al., 2017). This was confirmed in recent work by Browning and Sawyer (2021) who classified about 88 % of the tropical region as having medium to high vulnerability to erosion. However, past assessments are mostly based on global soil erosion and sediment transport models that are not yet well constrained for the tropical region because of data scarcity (Shahgedanova et al., 2021). This is particularly the case in tropical mountain regions, where the availability of empirical data is limited in time and space (Rosas et al., 2020; Vanacker et al., 2020).

The tropical Andes has been less studied in terms of hydrometeorology and erosion processes, in comparison to other major mountain ranges in the world (Vanacker et al., 2007; Pepin et al., 2010). Its impressive length, continuity and height significantly disrupt the atmospheric circulation resulting in a wide variety of environmental conditions (Garreaud, 2009; Poveda et al., 2020). Environmental gradients are steepest along the western flank of the Andes that is characterized by marked differences in vegetation, rough topography with deeply incised canyons, and highly variable and extreme precipitation patterns (Tote et al., 2011). These environmental conditions pose particular challenges for erosion and sediment flux monitoring (Vanacker et al., 2020). Moreover, the connectivity between the sources of sediment (e.g., rill and gully erosion, landsliding, bank erosion) and the river network is not well studied. Temporary or permanent sediment storage, erosion and remobilisation can occur across the river system, and affect the transfer of sediment from hillslopes to floodplains and river channels. Recent studies on the western Andes (Martini et al., 2020; Restrepo et al., 2020; Vergara et al., 2022) illustrated how sediment connectivity can modulate the geomorphic response to disturbance events, and the importance for catchment management and risk assessment.

Previous efforts were mostly focused on sediment fluxes in large rivers draining to e.g. the Amazon basin (e.g. Armijos et al., 2013; Vauchel et al., 2017) while small to medium-sized rivers such as the ones flowing towards the Pacific Ocean have been relegated (Latrubesse and Restrepo, 2014). Most of them are undocumented: in the global dataset of Milliman and Farnsworth (2011), only 450 of the approximately 23 000 rivers correspond to small- to medium-sized catchments (drainage areas between 100 and 3000 km^2), and only four of the 70+ documented rivers draining the western Andes contained sediment data, i.e. the Mira, Patia and San Juan rivers in Colombia (Restrepo and Lopez, 2008) and Chira River in Peru (Milliman and Farnsworth, 2011). Often, small to medium-sized rivers are sampled during a few years only to obtain an operational concentration-discharge curve; afterwards, sampling is reduced or stopped assuming no temporal change in sediment production and transport (Milliman and Farnsworth, 2011). The importance of studying sediment delivery from small and medium-sized catchment was highlighted in the global study of Harrison (2000) who showed higher than average sediment delivery in these catchments where erosion processes are enhanced due to steep hillslope and river gradients and higher coupling between hillslopes and river channels. Similar observations were made by de Vente et al. (2013) who concluded in their study on erosion models that more efforts are needed to constrain erosion rates in small to medium-sized catchment.

Sediment yields are commonly determined at sediment gauging stations, where data on water discharge and suspended sediment concentration are available. In the tropical Andes, extreme rainfall events during e.g. ENSO events can transport disproportionally large amounts of sediments, and high-frequency SSC monitoring is therefore required for reliable sediment yield estimates (Navratil et al. 2011; Vanacker et al. 2020). As an alternative to suspended sediment sampling, turbidity records are increasingly used to estimate sediment loads in the Andes. They offer the advantage of continuous monitoring, even during extreme flood events when the river valley is not accessible for sediment sampling (Lewis, 1996; Navratil et al., 2011; Ellison et al., 2014. López-Tarazón et al., 2009). However, permanent gauging stations with long time series of hydrometeorological records are scarce in the tropical Andes (Vanacker et al., 2020; Shahgedanova et al., 2021). Alternatively, information on reservoir sedimentation has been used to derive estimates of the total sediment yield of the upstream area, as periodic surveys of the bathymetry and/or topography of small ponds, reservoirs or lakes can provide information on the volume of sediment accumulated over a given time period (Molina et al., 2008; Vanacker et al., 2015; Verstraeten and Poesen, 2002). Such estimates of sediment deposits include the material transported in the river system as suspended and bedload.

Sediment yield is controlled by environmental and/or anthropogenic factors (Kemp et al., 2020). Numerical models based on global datasets, such as BQART (Syvitski and Milliman, 2007) or stream-power models (Crawford, 1991), can provide first insights in the controlling factors (e.g., Campforts et al., 2020). Based on a global assessment, Syvitski and Milliman (2007) concluded that geological factors (relief, area, and lithology of the catchment) explain 65 % of the variation in sediment yield whereas climatic and anthropogenic factors collectively explain an additional 30 % of the variability. When focusing on regions with few observational data, direct application of geomorphic transport laws is not straightforward. Following the Tropical Andes from north to south, the specific sediment yield ranges from 5 to 1150 t km^{-2} yr^{-1} (Moquet et al., 2020; Restrepo et al., 2009; Tenorio et al., 2018; Vanacker et al., 2007). These authors attributed the observed variation in specific sediment yield to multiple environmental factors amongst which mean annual runoff, relief ratio, lithology and catchment area (Restrepo et al., 2006; 2009; Vanacker et al., 2015; Litty et al., 2017) and land use and management (Molina et al., 2008; Restrepo et al., 2015). Exceptionally high values are reported for northern Peru where El Niño Southern Oscillation (ENSO) events strongly control the temporal variation in sediment fluxes. The sediment yields during moderate ENSO events are estimated to be 5 to 11 times the rates during normal rainy seasons (Tote et al., 2011), and up to 60 times' increases are reported during extreme events resulting in sediment fluxes up to 1000 and 3000 t km^{-2} yr^{-1} (Morera et al., 2017). In the Chilean Andes, south of the Tropical Andes, the spatial distribution of specific sediment yield is more uniform with rates generally below 700 t km^{-2} yr^{-1} (Pepin et al., 2010; Carretier et al., 2013). Here, topography and vegetation cover are being identified as the main controlling factors (Pepin et al., 2010; Tolorza et al., 2014).

Within the Tropical Andes, there is a clear gap in observational data on sediment yield for the western flank of the Andes Mountains (Rosas et al., 2020). A recent systematic review by Vanacker et al. (2022) on water erosion in the Andes identified critical gaps in knowledge and research on soil erosion and sediment yield, and a need for empirical work on erosion and sediment yield in data-scarce regions such as e.g. areas with very low to low precipitation. Of the 132 documented case-studies, only 8 studies included data on the western margin of the Andes. This region, particularly along the coasts of southern Ecuador and Peru, is characterised by torrential and extreme precipitation events (Litty et al., 2017; Rau et al., 2017) leading to landslides, mud- and debris flows, reactivation of gully systems and flooding of alluvial and coastal plains (Romero et al., 2007; Tote et al., 2011). This was observed during the rainy season of 2018–2019 when a multitude of geomorphologic-related disasters caused damage to critical infrastructure, water supply and sanitation, hydropower generation and local economy (INDECI, 2012; 2017; ENFEN, 2017). For example, Morera et al. (2017) estimated that 60 % of the storage capacity of the Poechos reservoir was lost over the past 36 years due to reservoir sedimentation during two extreme ENSO events. It is expected that the vulnerability to natural hazards will further increase over the next decades due to increasing climate variability (Poveda et al., 2020).

In response to this state of knowledge, our study addresses the following questions: (1) How is the specific sediment yield changing along the western flank of the Peruvian Andes?; and (2) Which environmental factors are associated with the spatial variation in specific sediment yield? We first compiled a new dataset that comprises published and unpublished information from river gauging stations, water quality monitoring, and reservoir sedimentation of 21 catchments distributed over the Peruvian western Andes. Based on these preliminary results, we studied environmental data over 30-years period (1990 – 2019) on climate, water discharge, lithology, topography and vegetative cover were obtained from satellite-based products to fill gaps in local databases. We carried out statistical correlation and univariate and multivariate regression analysis to study the association between specific sediment yield and environmental variables in the region.

2. Study area

2.1. Topographic and geological setting

The catchments are located along the western flank of the tropical Andes between 3° and 14.5° South (Fig. 1). Its northern part (between 3°and 6° S) is characterised by a large coastal plain that extends 100 km from the Pacific Ocean to the western Cordillera, and an altitude varying between 0 m along the coastline and 2500 m a.s.l. in the headwaters. The area is underlain by siliciclastic and mixed sedimentary rocks, unconsolidated Quaternary sediments in the coastal plain and intermediate volcanic and acid plutonic rocks in the upper catchment with some metamorphic rocks (Hartmann and Moosdorf, 2012). The coastal plain becomes much narrower, i.e. up to 10 km width, in the central part between 6° and 11° S. In this region, the topographic relief increases from 0 to 100 m a.s.l. in the coastal plain to a mean altitude of 3000 m a.s.l. in the western Cordillera with peaks up to 6000 m. This region is characterised by Cretaceous acid plutonic and intermediate volcanic rocks, with Paleogene-Neogene mixed sedimentary rocks in the headwaters. South of 11° S, the coastal plain becomes very narrow. The escarpment of the western Cordillera has a steep gradient between 11° and 14.5° S, with an average elevation of 4000 m a.s.l. Cretaceous acid plutonic and intermediate volcanic rocks and unconsolidated sediments are dominant, but outcrops of pyroclastics and carbonate sedimentary rocks can also be found.

2.2. Soils and geomorphology

Arenosols are the predominant soil type along the western flank of the Peruvian Andes (Gardi et al., 2015). Arenosols are developed on sand-rich parent material, and characterised by weak profile development, low water holding capacity and poor nutrient content. In the northern part (3° – 6° S), they cover 50 % of the area. Cambisols and Leptosols are the main remaining soil groups that prevail at altitudes of 1800 to 3500 m, with the former being sandy soils with initial soil formation with at least one subsurface horizon and the latter being shallow soils developed on hard rock or gravelly material (Gardi et al., 2015). During intermittent or torrential rain events, soils and sediments can be mobilised on the hillslopes by overland flow, and transported as mud and debris flows to the river network (Mettier et al., 2009). Most of the deposits of sediments in the alluvial plains are related to dry river courses or gullies that can be activated during the wet season (Luque et al., 2020), and extreme rainfall events (Tote et al., 2011). Likewise, the predominant soil groups in the central and southern regions (6° – 14.5° S) are Arensols and Leptosols, while Fluvisols can be found in areas of recent alluvial or marine deposits that are exposed to periodic flooding (Gardi et al., 2015). The fluvisols are found in the floodplains, and may contain significant amounts of humus in the upper parts. The central and southern region is prone to soil erosion by water, including active gullying (e.g., Inbar and Llerena, 2000), and mass movements (Harden, 2006; Luque et al., 2020).

2.3. Climate and land cover characteristics

In the northern part (3° – 6° S), there exists a clear contrast in precipitation amounts and regimes between the coastal plain, mountain foothills and headwaters. In the coastal plain, the average annual precipitation is 90 mm yr^{-1}: about 90 % of the annual precipitation falls from January to May. During strong ENSO events (1982–83 and 1997–98), the precipitation reaches peaks of 1000 mm yr^{-1}. The mountain foothills have an average precipitation of 370 mm yr^{-1}, but show high monthly variability of precipitation amount in the wet season (January to April). The variability is caused by ENSO events (reaching precipitation rates higher than 2700 mm yr^{-1}) and local convective

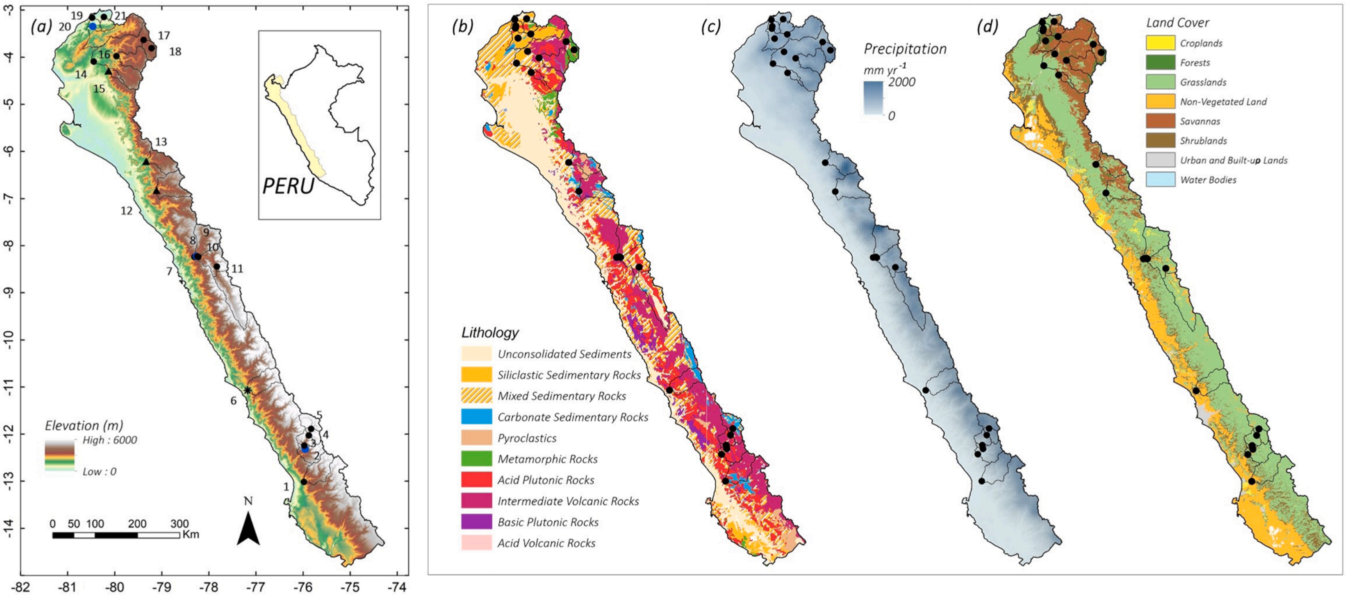

Fig. 1. Spatial distribution of the 21 catchments in the Peruvian western Andes. (a) Topography of the region extracted from Lehner et al. (2008). The circles show the location of the outlet of the catchments, and their colour/shape indicates the data type (SSC: suspended sediment concentration, RT: rating curve, TU: turbidity and BAT: sediment storage in reservoirs). (b) Lithology based on Hartmann and Moosdorf (2012) (c) Average annual precipitation based on Aybar et al. (2017). (c) Land cover of 2018 based on Friedl and Sulla-Menashe (2019).

storms mainly related to the Kelvin waves. The mountainous headwaters are part of the bi-national Catamayo-Chira catchments, and have an average precipitation of 1024 mm yr^{-1}. About 70 % of the annual precipitation falls in the rainy season (January to April). The precipitation fluctuation is related to local convective events related to the Madden and Julian Oscillation. Vegetation patterns in the northern area are strongly linked to precipitation patterns. The coastal plain is barren with total vegetative cover below 10%, the mountain foothills have a dominance of annual grasses, herbs and shrubs (generally < 2 m high), and the headwaters are covered by savannas with a tree cover between 10 and 60 %, deciduous broadleaf forest and grasslands.

In the central and southern part (6° − 14.5° S), there is a remarkable difference in climate between the coastal plain and mountain foothills that are the driest region in Peru with an average annual precipitation of 16 mm yr^{-1} (Rau et al., 2017) and the mountainous headwaters. In the headwaters of the central part, the annual precipitation is 492 mm yr^{-1} (Rau et al., 2017). The rainy season runs from December to April but there is strong interannual variability in monthly precipitation, whereby the precipitation peaks are not related to strong ENSO events. South of 11° S, the headwaters have an average precipitation of 366 mm yr^{-1}, with 85 % of the annual precipitation falling during the wet season (December to March). The vegetation pattern is a result of the climatic conditions, with bare land and irrigated crops in the coastal plain and annual grasses and shrublands in the remaining areas (Fig. 1).

3. Materials and methods

3.1. Compilation of dataset on sediment yield

3.1.1. Data sources

We compiled data on specific sediment yield for 21 catchments distributed over the Peruvian western Andes (Table 1, Fig. 1). Data were obtained from public institutions in Peru and Ecuador (Superintendence of Services and Sanitation, SUNASS; National water management projects, PE, and National Institute of Meteorology and Hydrology, INAMHI), unpublished data from private companies (Abel Rodriguez; V&A Consulting Engineers) and recent publications by Oñate-Valdivieso and Bosque Sendra (2014), Morera et al. (2017) and Rosas et al. (2020). Sediment yields were derived from (i) data on suspended sediment concentration and discharge, (ii) water turbidity, (iii) published concentration-discharge curves and (iv) bathymetric data from human-made reservoirs (see Table 1 and Fig. 1). To constrain sediment yield variation over the western Andes, we focused on the time period 1990–2019 during which most observational data were collected (Table 1). We included four catchments (#11, 14, 16, 19, Table 1) that had exceptionally long time series extending beyond the envisaged time period (#11, 14, 16) or that covered important gaps in terms of spatial coverage (#19, Fig. 1).

To obtain the sediment yield over the 30-year time interval, we developed concentration-discharge curves based on suspended sediment concentration or turbidity data, and derived the average specific sediment yield based on reconstructed timeseries of discharge data (sections 3.1.2 and 3.1.3 respectively for more details). For the bathymetric data, we derived the specific sediment yield from the annual average sediment storage in the reservoir (see section 3.1.4).

3.1.2. Specific sediment yield derived from suspended sediment concentration or turbidity

3.1.2.1. Relation between suspended sediment concentration and discharge. For 14 catchments (Table 1, "SSC" catchments), we had detailed information from sediment gauging campaigns, that included data on

Table 1

Overview of the 21 study catchments, with indication of geographic location, catchment area, data period, frequency of sampling, and type and number of samples. The data types are classified as suspended sediment concentration (SSC), water turbidity (TU), concentration-discharge curve (RC), and bathymetric data (BAT).

ID	Station	River	Latitude (°)	Longitude (°)	Catchment area (km^2)	Data period	Sampling frequency	Data type	N° samples
1[g]	A1 – Conta	San Juan	−13.4371	−75.9708	3020	Apr. - Jun. 2019	~ 3 per month	SSC	6
2[a]	*C2* – Chavin	Cañete	−12.7450	−75.9445	3360	1998–2001	–	RC	–
3[a]	C3 – Putinza	Cañete	−12.6682	−75.9598	3120	Jan. - Mar. 2018	2 per day	SSC	72
4[a]	C4 – Huantan	Cañete	−12.4514	−75.8644	2200	Jan. - Mar. 2018	2 per day	SSC	70
5[a]	C5 – Azuchas	Cañete	−12.3110	−75.8140	1390	Jan. - Mar. 2018	2 per day	SSC	56
6[b]	H1 - Santo Domingo	Chancay Huaral	−11.4954	−77.1665	2750	2014–2018	1 per day	TU	1693
7[c]	S1 – Bocatoma Chavimochic	Santa	−8.6595	−78.2949	10 500	1999–2010	1 per day	SSC	3961
8[d]	S2 – Condorcerro	Santa	−8.6500	−78.2500	10 400	1999–2010	1 per day	RC	–
9[c]	S3 – Tablachaca	Tablachaca	−8.6476	−78.2319	3190	2003–2010	1 per day	SSC	2094
10[c]	S4 – Chuquicara	Santa	−8.6605	−78.2118	7170	2003–2010	1 per day	SSC	1630
11[g]	S5 – La Balsa	Santa	−8.8667	−77.8167	4290	1975–1989	~1 per week	SSC	617
12[c]	J1 – Yonan (Gallito Ciego)	Jequetepeque	−7.2500	−79.1000	3300	1991–2017	–	BAT	9
13[c]	L1 - Raca Rumi (Tinajones)	Reque	−6.6333	−79.3167	2370	1969–2017	–	BAT	14
14[e]	CC1 – Ardilla	Chira	−4.5167	−80.4333	11 900	1981–1992	1 per day	SSC	3147
15[c]	CC2 – Chipillico (San Lorenzo)	Chipillico	−4.7144	−80.1184	490	1960–2008	–	BAT	3
16[f]	CC3 - Puente Internacional	Macara	−4.4003	−79.9503	2460	1972–1992	1 per day	SSC	6178
17[e]	CC6 – Arenal	Catamayo	−4.0544	−79.3736	1160	1977–2006	1 or 2 per year	SSC	23
18[e]	CC7 – Uchima	Catamayo	−4.2303	−79.2036	47.7	1977–1991	1 or 2 per year	SSC	10
19[b]	T1 – Puente Tumbes	Tumbes	−3.5833	−80.4667	5290	2014–2018	2 per year	SSC	7
20[d]	T3 - El Tigre	Tumbes	−3.7687	−80.4566	4690	2004–2012	–	RC	–
21[b]	Z1 – Bocatoma La Palma	Zarumilla	−3.5667	−80.2167	787	2014–2016	2 per year	SSC	5

Sources: [a] Rosas et al., 2020. [b] SUNASS, Superintendence of Services and Sanitation. [c] PE, National water managment projects (Cha vimochic, Jequetepeaue Zaña, Olmos Tinajones and Chira Piura). [d] Morera et al., 2017. [e] INAMHI, Ecuadorian Hydrology and Climate office. [f] Oñate-Valdivieso and Bosque Sendra, 2014. [g] Private company data.

suspended sediment concentration and discharge at the time of sampling. The suspended sediment concentration was determined on 0.5 or 1 l water samples, that were treated according to the existing protocols at the official instances (SUNASS or INAMHI). The discharge was derived from water height measurements (on a graduated scale at the gauging station) using the existing rating curves, or from discharge measurements with a current meter in the case of the San Juan River at Conta (Table 1).

For these locations, the average specific sediment yield was derived based on the sediment concentration – discharge curve, which is the correlation between the suspended sediment concentration of a water sample (SSC, in g l^{-1} or kg m^{-3}) and the discharge (Q, m^3 s^{-1}). The curve is typically calculated by linear regression in log space: $\log SSC = \log \alpha + \beta \log Q$ where α and β are the regression coefficients (Crawford, 1991). Work by Harrington and Harrington (2013) showed that the conversion to log space and the subsequent de-transformation from log to normal space increases bias in the SSC estimates. Therefore, some authors (e.g. Asselman, 2000; Khaleghi and Varvani, 2018) suggested to apply power regression, $SSC = \alpha\ Q^{\beta}$, especially when the input data show strong differences in sediment dynamics between the rainy and dry seasons (Harrington and Harrington, 2013). The hydrological regime in the catchments draining the Peruvian western Andes has unimodal distribution, and, therefore, the sediment load is predominant in the wet season. Thus, a power fit (Eq. (1)) was applied to the dataset (SSC and Q), using least-square distance criteria for minimizing errors. The regression has the form:

$$SSC = \alpha Q^{\beta} + \frac{\sigma^2}{2} \tag{1}$$

where α and β are the coefficients to fit the power law equation and σ is the residual standard error. The goodness of fit was assessed by the residual standard error (RSE), the determination coefficient, R^2, and p-value. Given the limited number of sediment data, and the important gaps in the sediment record, we applied bootstrapping techniques to better constrain the overall uncertainty on the sediment yield estimates (see more details in section 3.1.2.4). For 3 catchments (Table 2.1, “RC” catchments), we had information on the sediment rating curve from previously published work (Rosas et al., 2020; Morera et al., 2017).

3.1.2.2. Relation between water turbidity and suspended sediment concentration. For one catchment (Table 1, “TU” catchment), we had detailed information on temporal variations in water turbidity based on measurements collected over the time period 2014–2018. However, for the site, no local calibration of the turbidity sensor was available. We revised existing SSC-turbidity relations from literature (Lewis, 1996; Navratil et al., 2011; Ellison et al., 2014) to transform the turbidity values into suspended sediment concentrations. Previous work by Lewis (1996) showed good agreement between turbidity and suspended sediment concentration for a small mountain catchment in northern California, with model errors between 2 % and 8 %. Similar results were observed in the southern French Alps with an average uncertainty of ~ 10 % in the SSC estimations (Navratil et al., 2011).

The turbidity study by Ellison et al. (2014) on selected rivers in Minnesota (USA) best represented the turbidity data for the Chancay-Huaral catchment (#6, Table 1). The Minnesota data include 314 samples of SSC and turbidity in nephelometric turbidity ratio units (NTU) for the years 2007 to 2011. The turbidity data included values between 1 and 990 NTU representing at the same time low and high turbidity values, reducing the possibility of overestimation of high values. The following power regression model ($R^2 = 0.74$, p-value < 0.01) for the SSC-turbidity relation was established based on the dataset of Ellison et al. (2014):

$$SSC = 3.70 * 10^{-3} * Turbidity^{0.85} \tag{2}$$

The turbidity data expressed in NTU of the Chancay-Huaral catchment were converted into suspended sediment concentrations (g l^{-1}) using equation (2). Then, the method described in section 3.1.2.1 was used to derive the sediment rating curve, which is the relation between the suspended sediment concentration (SSC, in g l^{-1} or kg m^{-3}) and the discharge (Q, m^3 s^{-1}).

3.1.2.3. Reconstructed timeseries of river discharge. For the 18 catchments with information on suspended sediment concentration, sediment rating curve or turbidity, we collected daily timeseries of river discharge (Q, m^3 s^{-1}). Data were extracted from the observational database of the Peruvian National System of Hydric Resources (Sinrh), which contains daily discharge information from a network of hydrological stations. Although quality and quantity of available observational data improved in the last decade, there are important gaps in the discharge records over the period 1990–2019. Therefore, we filled gaps with information from the GloFAS-ERA5 global river discharge dataset (Harrigan et al., 2020). The GloFAS System provides gridded daily river discharge data, with a resolution of 0.1° x 0.1° (~11 km × 11 km). The data covers the period from January 1st 1970 until now, and is updated almost instantaneously so that it can deliver near real-time data. The database has been used for global flow estimations (Dottori et al., 2016; Alfieri et al., 2020), and has been used previously for Peruvian rivers by Bischiniotis et al. (2019).

The GloFAS-ERA5 dataset and the hydrological data from the gauging stations show similar temporal patterns in river discharge, but there exists a systematic offset in daily river discharge due to underestimation of the peak discharge in the GloFAS-ERA5 dataset. Therefore, direct gap filling was not possible. To correct the gridded data for this systematic bias, we made a linear regression between both datasets, $y = ax + b$, where $b = 0$ to avoid the shift in the hydrographs. The coefficient of determination (R^2) between the observed and the gridded discharge data was calculated to assess the downscaling performance. Then, this site-specific regression equation was applied to the GloFAS-ERA5 river discharge product to obtain bias-corrected daily discharge for the 18 locations. These data were then used to complete the time series of the hydrological stations. From the gap-filled daily discharge data of each station for the 1990–2019 period, two variables were extracted for further analyses: the quantile 50 (Q_{50}) and quantile 90 (Q_{90}). The former represents the median discharge, and the latter is an estimate of the discharge during storm events.

3.1.2.4. Uncertainty analysis of sediment yield data. To account for the uncertainty on the sediment rating curve, a bootstrapping approach was applied, with resampling of individual observations with replacement (Wilks, 2019). The replacement was limited to max. 10 % of the original dataset, and 100 resamples were done per station for the reconstruction of the concentration – discharge relationship using power law regressions (Eq. (1)). We used the regression equations to obtain a continuous record of suspended sediment concentrations. Then, continuous timeseries of daily solid discharge, Q_s (kg s^{-1}) were obtained by multiplying the daily discharge, Q, by the estimated suspended sediment concentrations obtained from the 100 power law regressions. For the 100 simulations, the daily data were then aggregated at annual timestep, and the mean annual sediment yield was calculated for the period 1990–2019. From the simulations, an ensemble means, and the 95 % confidence interval was derived for the mean annual sediment yield and the specific sediment yield (SSY, t km^{-2} yr^{-1}).

3.1.3. Sediment yield derived from bathymetric data

For three catchments (Table 1, #12, 13 and 15), bathymetric data was available from reservoirs. In all three cases, the information was derived from standard bathymetric surveys during which measurements on the water depth were realized with a single-beam echosounder from a boat that was precisely geolocated with GPS receivers. These data allow to reconstruct the sediment volume that is deposited in the reservoir over a given amount of time. For the three reservoirs for which data were available, the inventories cover a time period of 26 to 48 years. We collected information on 9 bathymetries in Gallito Ciego reservoir (#12) that were carried on between 1991 and 2017, 14 (annual) bathymetries in Tinajones reservoir (#13) and 3 bathymetries in San Lorenzo (#15) reservoir that were realized every 10 years. From the sediment volumes, the specific sediment yield of the contributing catchments, SSY (t km^{-2} yr^{-1}) can be derived as follow:

$$SSY = 100\frac{SR*BD}{STE*A} \quad (3)$$

where SR is the average annual sediment volume accumulated in the reservoir from the bathymetric data (m^3 yr^{-1}); BD the dry sediment bulk density (t m^{-3}); STE the sediment trap efficiency of the reservoir (%); A the catchment area (km^2). The bulk density of the sediment trapped in the reservoirs #12, #13, and #15 is 0.98, 1.35 and 1 t m^{-3} respectively. The model from Heinemann (1981) was applied to correct the sediment volumes for incomplete sediment retention in the reservoir, as this model is suitable in contexts with limited data availability. The empirical model relates the STE to the ratio of the reservoir storage capacity C (m^3) over the average annual river inflow, I (m^3):

$$STE = -22 + \frac{119.6\frac{C}{I}}{0.012 + 1.02\frac{C}{I}} \quad (4)$$

The rivers draining the western Peruvian Andes predominantly transport sand and gravel during high flow events. Unpublished data show that sands are predominant in the suspended fraction, and that medium and coarse gravels dominate in the bedload material. Given the coarse nature of the sediments, and the low organic matter content, we did not account for compaction in our sediment yield estimates. The uncertainty on the specific sediment yield, δSSY, results from the error on the bathymetric surveys and the error on the annual river inflow. The latter is similar to the before-mentioned error on the discharge measurement ($\delta Q/Q = 10\%$). The former error on the bathymetric surveys is the result of position uncertainty expressed by a horizontal (δH) and vertical error (δV). The international standard for hydrographic surveys (IHO, 2008) sets the maximum error values based on the total depth of the reservoir (d) and the under-keel-clearance of the ship that performs the survey (the vertical distance between the bottom of the ship and the riverbed). For reservoirs shallower than 100 m, equations (5) and (6) were applied to obtain relative errors with a 95 % confidence level:

$$\delta H = 5 + 5\%d \quad (5)$$

$$\delta V = \pm\sqrt{0.25 + (0.013 + d)^2} \quad (6)$$

3.2. Environmental factors

The physical and environmental characteristics of each catchment were described by 22 variables (Table 2). The variables were derived for

Table 2
Description of the analysed environmental factors.

Type	Symbol	Unit	Description
Physical Variables	Z	m	Catchment average altitude
	A	km^2	Catchment area
	AvgS	%	Average catchment slope
	R	m	Relief, difference between the max. and min. elevation
	ks$_{25}$	log	Steepness index 1st quantile
	ks$_{50}$	log	Steepness index 2nd quantile
	ks$_{75}$	log	Steepness index 3rd quantile
Precipitation patterns	AvgP	mm yr^{-1}	Mean annual precipitation
	MaxP	mm month^{-1}	Mean maximum monthly precipitation
	P$_{95}$	mm	Precipitation on the wet days in the study period
	P$_{99}$	mm	Precipitation on the very wet days in the study period
	Ppk	–	Precipitation peakedness
Discharge patterns	Q$_{50}$	m^3 s-^{1}	50 % discharge percentile
	Q$_{90}$	m^3 s^{-1}	90 % discharge percentile
Lithological strength	L$_L$	–	Lithological composition index
	L$_E$	–	Lithological erodibility index
Land cover and vegetation changes	%G&Sh	%	Area cover by Grasslands and Shrublands
	%C	%	Area cover by Croplands
	%F&Sa	%	Area cover by Forest and Savannas
	% U&noV	%	Urban and Non-Vegetated Lands
	%Vinc	%	Area with an increase of vegetation
	%Vdec	%	Area with a decrease of vegetation

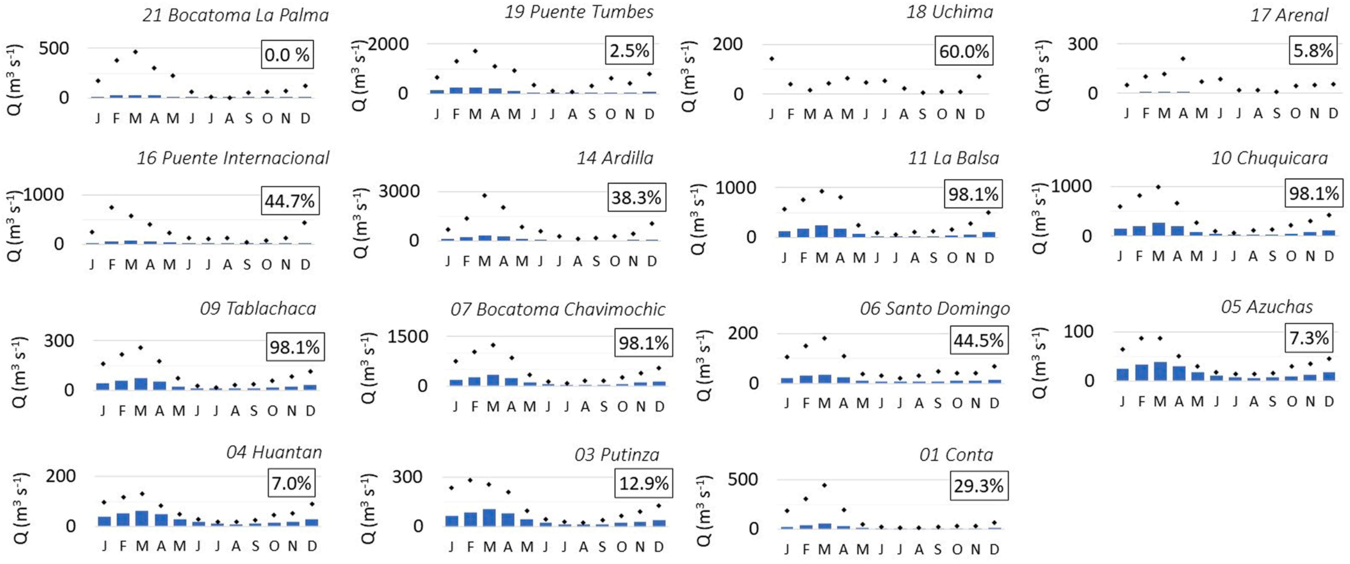

Fig. 2. Distribution of the monthly discharge for the study period (1990 – 2019). The blue bars show the mean monthly discharge Q (m^3 s^{-1}) and the black diamonds show the maximum values. The percentages in the corner of the figures report the proportion of observed river flow data that existed for a given station. Data gaps were filled using downscaled GloFAS-ERA5 river discharge product. (For interpretation of the references to colour in this figure legend, the reader is referred to the web version of this article.)

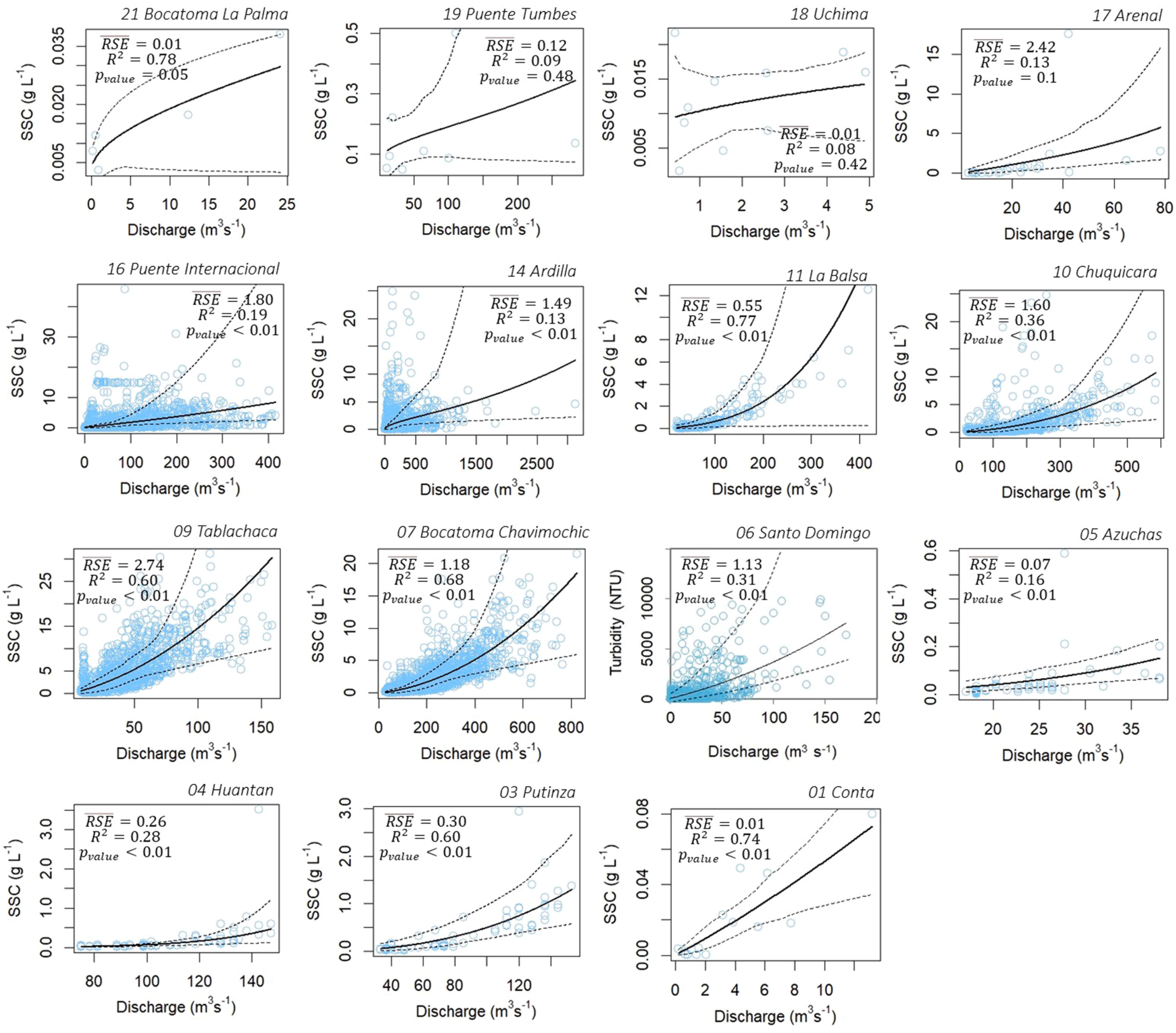

Fig. 3. Concentration-discharge curve obtained for the SSC and TU gauging stations. The black line represents the ensemble-mean curve and the dotted lines the 95 % confidence interval. The figure shows the average of the residual standard errors (RSE), the average determination coefficient (R^2) and p-values from the bootstrapping analysis.

the area upstream of the sampling station. They included seven physical variables, five meteorological and two hydrological variables, two variables for lithological strength and nine for land cover.

3.2.1. Physical variables

The physical variables were derived from a Digital Elevation Model. The Shuttle Rader Topography Mission (SRTM) has been shown to represent reliably the drainage network in the Peruvian Andes (González-Moradas and Viveen, 2020). We used the HydroSHEDS elevation model (Lehner et al., 2008), that is available at pixel resolution of 3 arc second (~90 m). The dataset is void-filled facilitating the derivation of continuous hydrological networks. The Toolbox of ArcMap 10.4 was used to extract the catchment-average altitude *Z* (m); the catchment area *A* (km^2); the average hillslope gradient *AvgS* (%); and the relief *R* (m) for each catchment. The river steepness index *ks* was calculated using the integral method proposed by Mudd et al. (2014). This method is available in the Chi Mapping Package of LSD TopoTools (Mudd et al., 2018). To represent the variation in river steepness along the river channel, we derived the 1st, 2nd, and 3rd quantile of the river steepness values (ks_{25}, ks_{50} and ks_{75}, respectively).

3.2.2. Precipitation patterns

Precipitation data were derived from the daily precipitation (mm day^{-1}) of the Peruvian meteorological institute (SENAMHI) Climatological and hydrological Observations (PISCO) product (Aybar et al., 2017; Aybar et al., 2020). PISCO has a 5-km pixel resolution and covers the period from 1981 to 2016. The data has shown a good performance when using monthly values, showing the highest correlation with field-based observations for the coastal Peruvian region (Aybar et al. 2020). For every catchment, we calculated the spatially averaged daily precipitation. From this dataset, we derived the mean annual precipitation, AvgP (mm yr^{-1}) and the mean maximum monthly precipitation, MaxP (mm $month^{-1}$). In order to represent the extreme events, we calculated the sum of precipitation in the “wet days” corresponding to the upper 5 % of the daily precipitation values (or P_{95}, 95th percentile of daily precipitation records), and the very wet days corresponding to the upper 1 % of the daily precipitation values (or P_{99},the 99th percentile of daily precipitation records). Finally, we obtained an index representing the intensity of precipitation events as precipitation peakedness, Ppk (Eq. (7)):

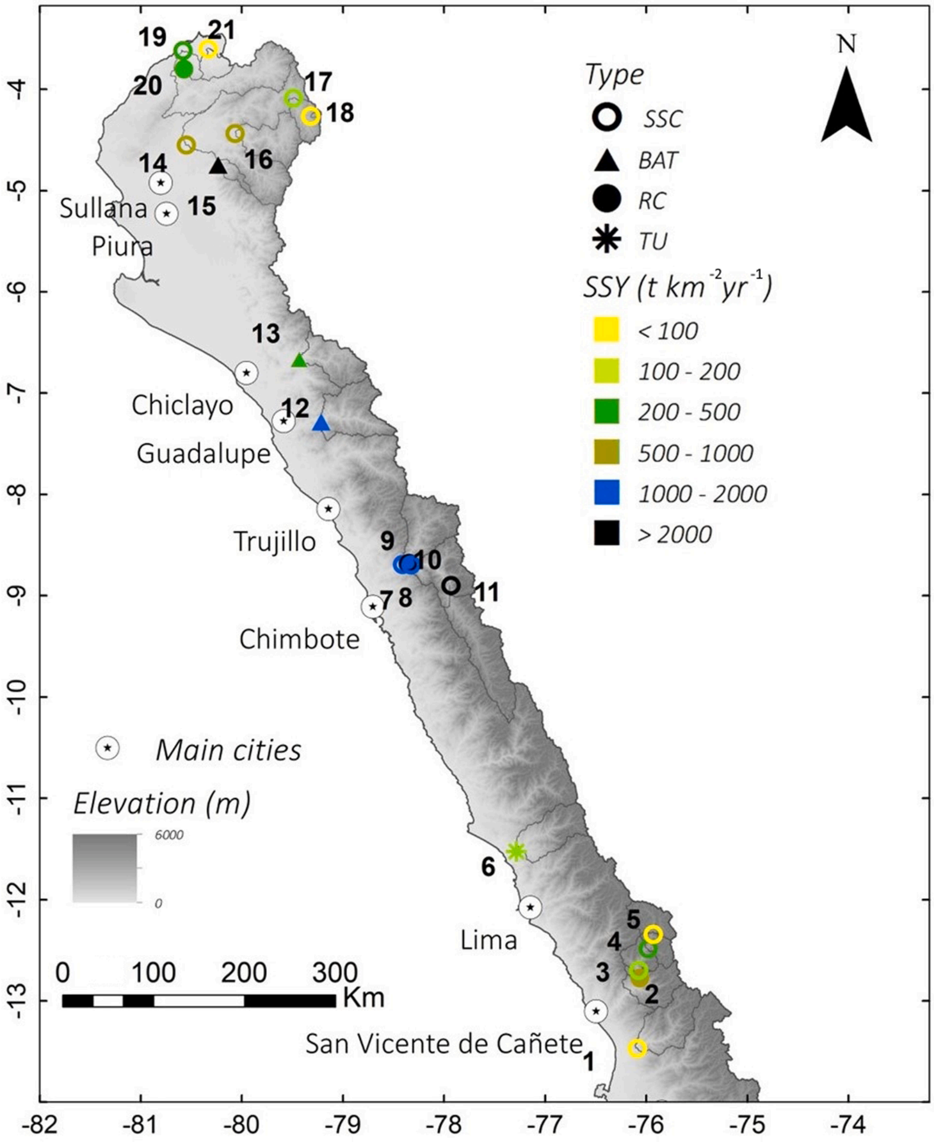

Fig. 4. Spatial distribution of the specific sediment yield (SSY) in the Peruvian western Andes. The dots are coloured by SSY, and their shape indicates the data type (SSC: suspended sediment concentration, TU: water turbidity, RC: concentration-discharge curve, and BAT: bathymetric data).

$$Ppk = \frac{MaxP}{AvgP} \tag{7}$$

3.2.3. Lithological strength

The lithological strength was evaluated based on the lithological erodibility index (L_E) proposed by Campforts et al. (2020). This index is calculated as:

$$L_E = \frac{2}{7}L' \tag{8}$$

$$\begin{aligned} L' &= \frac{L_A + L_L}{3} \; \textit{for non-igneous rocks;} \\ L' &= \frac{L_L}{2} \; \textit{for igneous rocks} \end{aligned} \tag{9}$$

Where L_A is a dimensionless erodibility index based on stratigraphic age, and L_L is a dimensionless erodibility index based on lithological strength similar to the erodibility index published by Aalto (2006). The L_L, ranges between 1 (igneous rock) to 12 (unconsolidated sediments) based on previous studies (Aalto et al. 2006; Campforts et al., 2020). We used the Global Lithological Map of Hartmann and Moosdorf (2012) that includes local geological information from Peru. The L_A is based on the stratigraphic age of non-igneous formations assuming higher degrees of diagenesis and increased lithological strength for older formations (following Kober et al., 2015). The L_A varies between 1 (Carboniferous) and 6 (Quaternary). Information for L_A is based on the Peruvian Geological map of INGEMMET (2016) that includes detailed chrono-stratigraphic information on the geological formations.

3.2.4. Land cover and vegetation changes

Land cover data was derived from the Moderate Resolution Imaging Spectroradiometer (MODIS) MCD12Q1 Product with 500 m spatial resolution (Friedl and Sulla-Menashe, 2019). In this product, the land cover is classified based on the annual leaf area index and the annual land cover maps are available for the period 2011–2018. Subsequently, ten land cover classes were distinguished including four forest types. We regrouped the information in four classes and calculated the catchment-average percentage of Grasslands and Shrublands (%G&Sh), Croplands (%C), Forest and Savannas (%F&Sa), and Urban and non-Vegetated Lands (%U&noV) for the time period 2011–2018. Likewise, we calculated the percentage of the catchment having vegetation increase (%Vinc) and decrease (%Vdec) over the 2011–2018 period.

Table 3
Summary of discharge, mean sediment yield, mean specific sediment yield (and the lower and upper bounds based on 95% confidence interval) per station for the period 1990–2019.

ID	Station	Area	Discharge ($m^3\ s^{-1}$)		Sediment yield	Specific Sediment yield ($t\ km^{-2}\ yr^{-1}$)		
		km^2	Q_{50}	Q_{90}	$x\ 10^3\ t\ yr^{-1}$	Average	Lower	Upper
1	A1	3020	9.38	44.9	237	78.6	13.2	247
2	C2	3360	36.0	120	1850	551	325	812
3	C3	3120	32.1	101	580	186	153	227
4	C4	2200	20.7	59.7	456	207	169	252
5	C5	1390	13.5	37.2	54.6	39.4	25.0	61.5
6	H1	2750	10.4	33.0	543	197	106	337
7	S1	10 500	81.9	312	14 210	1360	860	2990
8	S2	10 400	81.9	312	10 700	1030	71.5	1540
9	S3	3190	18.9	66.4	6780	2130	1100	4450
10	S4	7170	63.1	245	7530	1050	374	2320
11	S5	4290	48.8	220	9870	2300	1 830	2780
12	J1	3300	17.2	90.7	4870	1480	1 210	1750
13	L1	2370	21.3	80.4	955	403	255	551
14	CC1	11 900	58.9	289	5960	500	302	874
15	CC2	490	5.98	33.0	6010	2330	1770	2900
16	CC3	2460	13.0	68.5	1500	611	342	1080
17	CC6	1160	2.26	8.51	214	184	46.3	484
18	CC7	47.7	0.90	3.30	0.61	12.7	8.06	15.7
19	T1	5290	56.8	250	1250	235	51.4	893
20	T3	4690	42.2	286	1060	225	4.79	609
21	Z1	787	2.73	26	15.8	20.0	1.08	47.9

3.3. Statistical analysis of factors controlling SSY

Given the large number of environmental variables, we first observed the correspondance between them by using Spearman's rank-order correlation. Rank correlation has the advantage of being robust to outliers and is not linked to the distribution of the data. Before the correlation analysis, all variables were normalised by rescaling the values between 0 and 1. Subsequently, we calculated the correlation between the specific sediment yield and the physical, hydrometeorological, lithological and land cover variables by means of the Spearman's coefficient r and tested for significance using the corresponding p-values.

Univariate and multivariate regression techniques were used to identify the environmental variables that are the best predictors of specific sediment yield. We applied a forward stepwise selection method

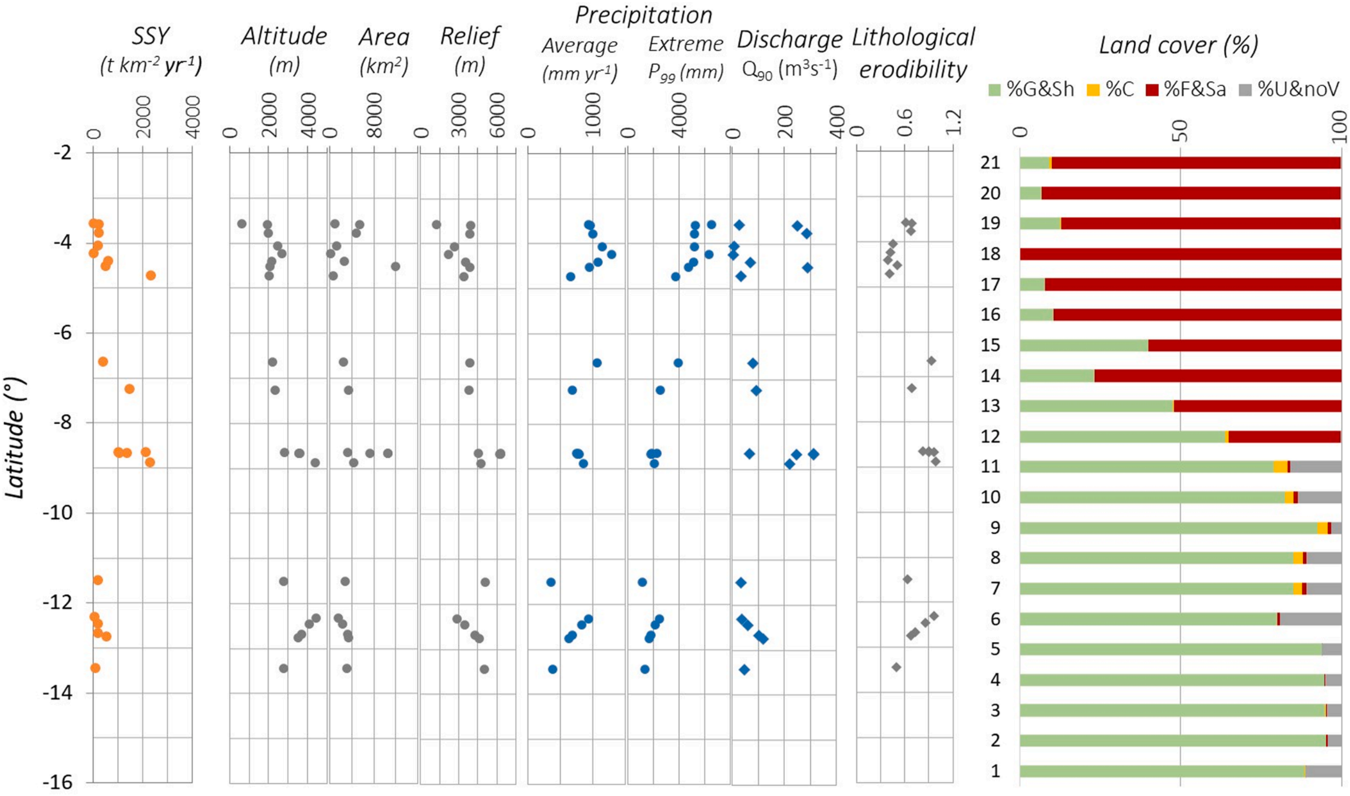

Fig. 5. Specific sediment yield (SSY) and environmental variables aggregated per catchment. The graphs show the latitudinal variation in SSY, mean altitude of the catchment, catchment area, mean hillslope gradient and relief, mean annual and precipitation on the very wet days, discharge (90th percentile), lithological erodibility index, and land cover distribution.

Table 4
Cross-correlation matrix. The values represent the Spearman's rank correlation coefficient between area (A), relief (R), river steepness index (ks_{50}), mean annual precipitation (AvgP), discharge (Q_{90}), the percentage of croplands (%C), sediment yield (SY) and specific sediment yield (SSY).

Variables	A	R	ks_{50}	AvgP	Q_{90}	%C	%F&Sa	SY	SSY
A	1.00	0.77	0.02	−0.19	0.94	0.49	− 0.13	0.73	0.48
R	0.77	1.00	0.46	−0.55	0.67	0.62	− 0.45	0.66	0.44
ks_{50}	0.02	0.46	1.00	−0.57	−0.09	0.37	− 0.36	0.22	0.24
AvgP	−0.19	−0.55	−0.57	1.00	−0.07	−0.33	0.68	−0.30	−0.31
Q_{90}	0.94	0.67	−0.09	−0.07	1.00	0.42	− 0.09	0.73	0.50
%C	0.49	0.62	0.37	−0.33	0.42	1.00	− 0.24	0.62	0.55
%F&Sa	−0.13	−0.45	−0.36	0.68	−0.09	−0.24	1.00	−0.10	−0.07
SY	0.73	0.66	0.22	−0.30	0.73	0.62	− 0.10	1.00	0.92
SSY	0.48	0.44	0.24	−0.31	0.50	0.55	−0.07	0.92	1.00

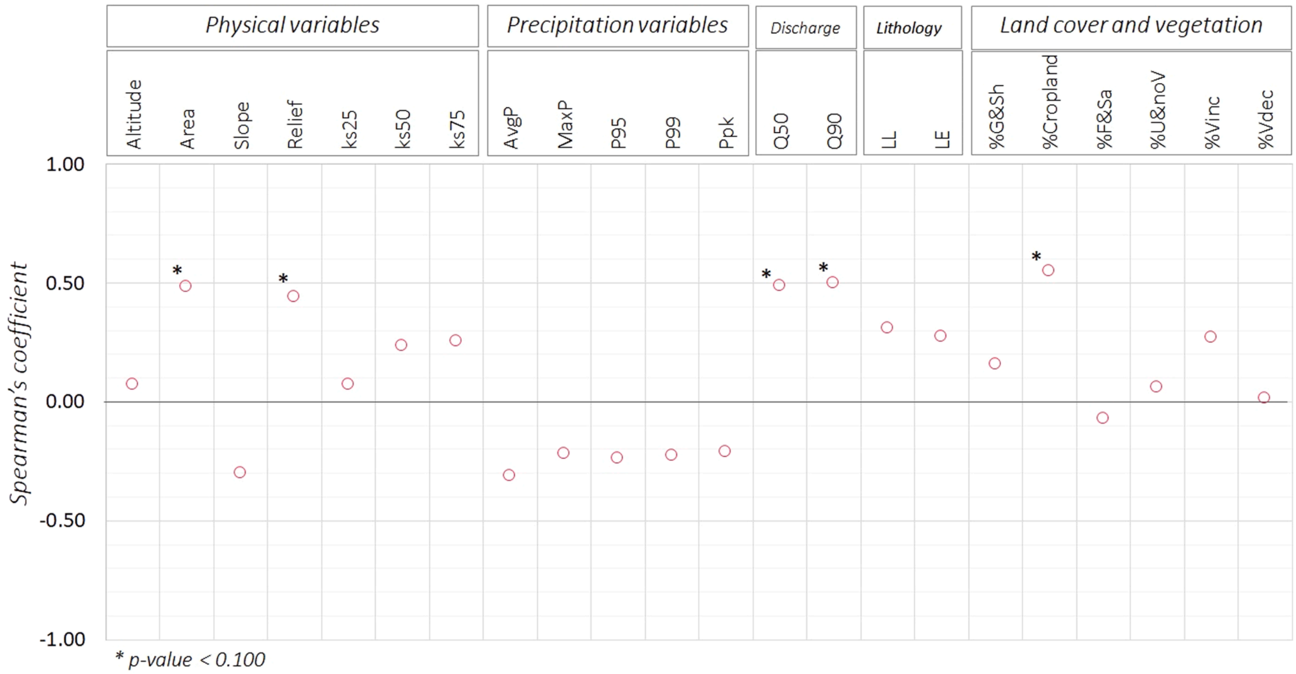

Fig. 6. Correlation between SSY and environmental variables represented by the Spearman's coefficient. The river steepness index (1st, 2nd, and 3rd quartile) is here represented as ks_{25}, ks_{50}, and ks_{75}; the mean annual precipitation as Avp; the mean maximum monthly precipitation as MaxP; the precipitation on the wet days and very wet days as P_{95} and P_{99}. the precipitation peakedness as Ppk, the 50th and 90th quantile of discharge as Q_{50}, Q_{90}; the lithological composition as LL and erodibility as LE; land cover classes and the increase and decrease of vegetation as %Vinc and %Vdec.

to build the regression models with the set of variables that are statistically most significant. Collinearity and multi-collinearity among explanatory variables were assessed from the Spearman's coefficient and the Variance Inflation Factor (VIF). The latter was used when three or more variables were included in the regression model, and measures how much the standard error of the model increased due to the collinearity (James et al., 2013). Here, we applied a VIF threshold of 5, and excluded variables from the regression when this value was exceeded. The predictive efficiency of the univariate and multivariate regression models was evaluated by a bootstrapping approach, after the selection of the best predictors. We resampled (with replacement) the dataset (21 points) 100 times to obtain a set of regressions and their corresponding coefficient of determination (R^2). The ensemble mean regression curve is reported, with the ensemble mean R^2 and 95 % confidence interval. The regression model was first built with the physical, hydrometeorological and lithological information only. At a second stage, the land cover information was included to test for improvement in model performance.

4. Results

4.1. Specific sediment yield estimates for the period 1990–2019

4.1.1. Uncertainty on the specific sediment yield estimates

The dataset of the Peruvian western Andes consists of 21 datapoints, for which the specific sediment yield over the period 1990–2019 was reconstructed based on newly established concentration-discharge curves for 14 stations, published concentration-discharge curves for 3 stations, turbidity-concentration-discharge relationships for one station, and bathymetric data for 3 catchments. By regional downscaling of the GloFAS-ERA5 product, we reconstructed daily time series of river discharge covering the 30-year period. In almost all cases, there is a good correlation between the observed discharge data and the gridded product with $R^2 > 0.40$ (see Suppl. Material S1). The mean monthly discharge (1990–2019) shows the unimodal distribution of the discharge over the hydrological year with peak discharges in March and low flow between June and October (Fig. 2). Downscaling the gridded data allowed us to obtain continuous time series, as important data gaps were present for sampling stations in the northern and southern part of the study region (corresponding to catchments # 4, 5, 17, 19 and 21 where more than the 90 % of the discharge information was missing,

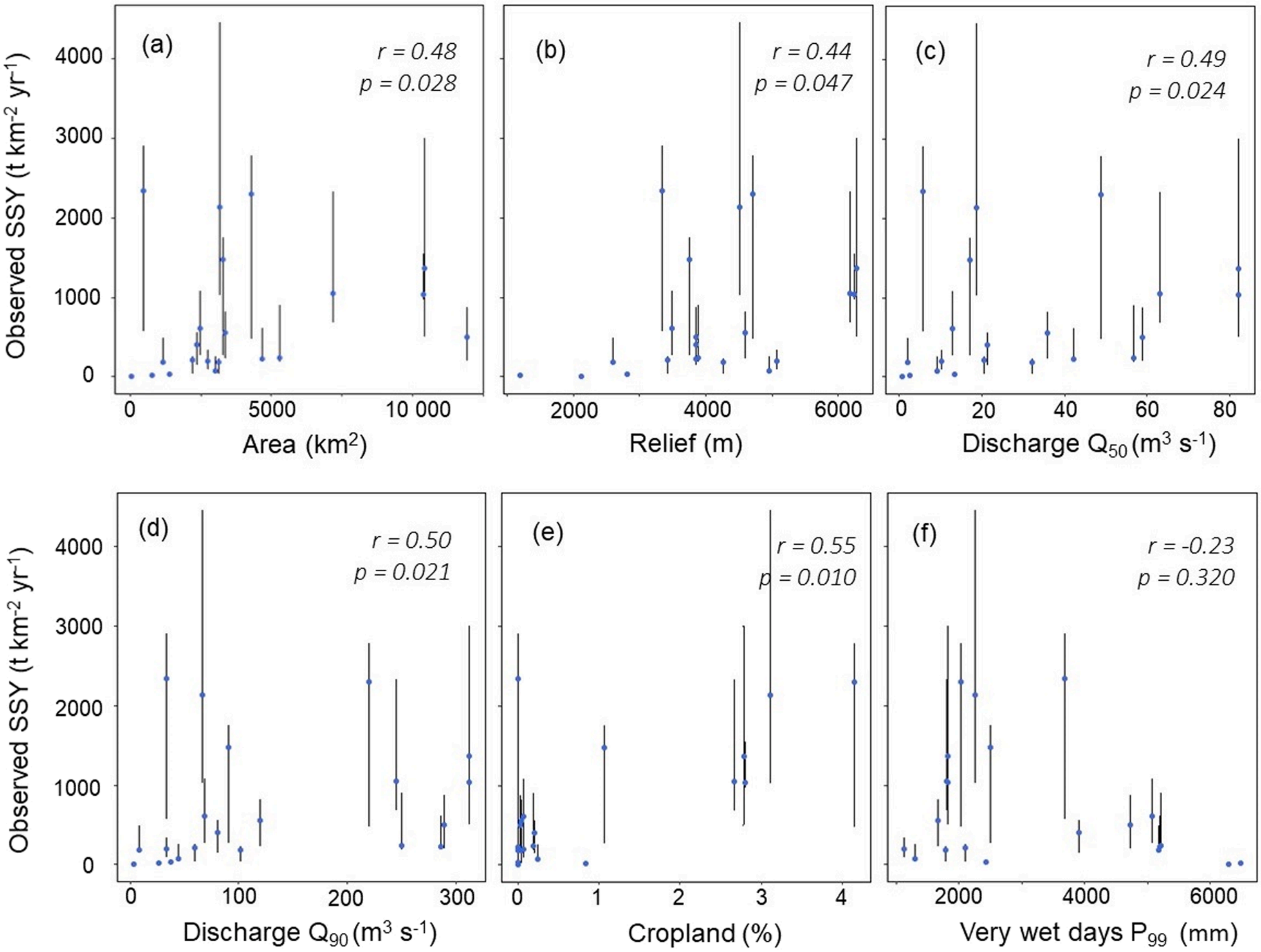

Fig. 7. Potential variables controlling specific sediment yield (SSY). Scatterplots between SSY and area (A), relief (R), discharge (Q_{50} and Q_{90} for 0.5 and 0.9 quantile respectively), percentage of cropland area (C%), and the precipitation on the very wet days (P_{99}). The plots present the Spearman's coefficient (r) and mention the p-value (p).

Table 5
Models (univariate, bi-variate, tri-variate) and estimators (R^2 and RSE), predicting the SSY in the study region. The included variables are area (A), discharge (Q_{50} and Q_{90}), relief (R), steepness (ks_{50}), runoff ($Q_{50}\ A^{-1}$), cropland percentage (%C), combination of grassland and shrubland (%G&Sh) and forest and savanna (%F&Sa).

Univariate model	R^2	RSE
$SSY = 1.20\ A^{0.76}$	0.34	0.24
$SSY = 1.57\ Q_{50}^{\ 0.65}$	0.38	0.23
$SSY = 1.49\ Q_{90}^{\ 0.66}$	0.37	0.24
$SSY = 1.10\ R^{0.84}$	0.45	0.22
Bi-variate model	R^2	**RSE**
$SSY = 0.78\ Q_{50}^{\ 0.59}\ ks_{50}^{\ 0.44}$	0.49	0.22
$SSY = 0.56\ Q_{90}^{\ 0.65}\ ks_{50}^{\ 0.55}$	0.55	0.20
$SSY = 0.86\ (Q_{90}A^{-1})^{0.15}\ R^{0.85}$	0.47	0.22
Tri-variate model	R^2	**RSE**
$SSY = 0.58\ Q_{90}^{\ 0.55}\ ks_{50}^{\ 0.52}\ \%C^{0.14}$	0.57	0.21
$SSY = 0.50\ Q_{90}^{\ 0.56}\ ks_{50}^{\ 0.49}\ \%G\&Sh^{0.20}$	0.56	0.21
$SSY = 0.26\ Q_{90}^{\ 0.70}\ ks_{50}^{\ 0.71}\ \%F\&Sa^{0.26}$	0.63	0.19

Fig. 2).

The reconstruction of the empirical relationships between sediment concentration and discharge (Fig. 3) is acceptable for the catchments in the central and southern part of the Peruvian western Andes (6° − 14.5° S). For most of these catchments (e.g., # 1, 3–7, 9–11), the suspended sediment samples are well distributed over the hydrological year including samples taken during dry and wet periods incorporating several peak events. For six catchments, the regression model is based on > 600 river water samples (Table 1). The goodness-of-fit is moderate to high for half of the catchments, with an ensemble-mean residual standard error (from the bootstrapping analysis) below 0.55 and a determination coefficient higher than 0.60. Lower performances correspond to catchments where the number of samples was limited (e.g. # 19 Puente Tumbes, RSE = 1.80, $R^2 = 0.09$; or # 17 Arenal, RSE = 2.42, $R^2 = 0.13$) or where we had to rely on published calibration curves to convert the turbidity values to sediment concentrations as no local calibration of the turbidity sensor was performed (e.g. #6 Santo Domingo, RSE = 1.13, $R^2 = 0.31$).

The northern part (between 3° - 6° S) lacks solid data on sediment fluxes, resulting in high uncertainty on the reconstructed specific sediment yields. On the one hand, there are catchments in the Chira-Catamayo catchment like #16 (Puente Internacional) or #14 (Ardilla) where intensive gauging campaigns were realized in the 1970 s and 1980 s resulting in respectively 6178 and 3147 data points. Notwithstanding the impressive amount of sediment samples, the relation between suspended sediment concentration and discharge is weak as exemplified by RSE values of resp. 1.80 and 1.49 (Fig. 3). On the other hand, there are catchments like #21 (La Palma), #19 (Puente Tumbes) or #18 (Uchima) where data on sediment concentration are scarce, and very low concentrations ($SSC < 0.2\ g\ l^{-1}$) were reported during the monitoring period. This is likely related to systematic undersampling during high or very high flows.

The bathymetric information corresponds to the main water reservoirs in the region. The uncertainty is related to the survey measurements and their frequency. The information in San Lorenzo reservoir (station #15) located in the northern area shows a SSY peak (2330 t km^{-2} yr^{-1}), the station compiles only 3 bathymetric surveys during the entire study period and the SSY error reach the 24 %. In the central area, the bathymetric data in the catchment #12 in Gallito Ciego reservoir, and 13 in Tinajones reservoir, is based in 8 and 13 bathymetric surveys respectively, and the results present errors under 20 % of the estimated SSY rate.

4.1.2. *Spatial pattern of specific sediment yield*

Our results do not show a marked spatial pattern in terms of specific sediment yield (Fig. 4 and Table 3). In the northern area (3° - 6° S), where catchments # 12 – 21 are located, the values oscillate widely between ~ 12.7 to 1750 t km^{-2} yr^{-1} (0.01 – 0.56 mm yr^{-1}). The highest sediment yield of 2330 t km^{-2} yr^{-1} (0.88 mm yr^{-1}) is observed in station # 15, San Lorenzo reservoir. In the central area (6° - 11° S), high SSY values of 2300 t km^{-2} yr^{-1} (0.87 mm yr^{-1}) were estimated for the upper catchment in the Santa basin (station # 11) and 2130 t km^{-2} yr^{-1} (0.80 mm yr^{-1}) in the Tablachaca stream located in the middle part of the basin (station # 9). The area south of 11° S (from station 1 to 10 in Fig. 4) has lower SSY values with values below ~ 1050 t km^{-2} yr^{-1} (0.40 mm yr^{-1}).

4.2. *Environmental factors controlling specific sediment yield*

4.2.1. *Latitudinal variation in environmental characteristics*

With exception of # 21 La Palma, the 21 catchments correspond to mountainous catchments, as the mean altitude of the upstream area is above 1900 m and the average hillslope gradient is between 15 and 60 %. Twenty of the 21 catchments correspond to large catchments with surface areas above 450 km^2, and three catchments are draining surfaces > 10 000 km^2. There is a wide range in river discharge, depending on catchment size and relief (see Suppl. Material S3), with mean annual flows between 1 m^3 s^{-1} and 82 m^3 s^{-1} and peak flows up to 308 m^3 s^{-1} in some of the larger catchments in the central and northern part of the study area.

The catchments cover the range in precipitation that exists along the Peruvian western Andes (Fig. 5), where the lowest value of mean annual precipitation (i.e., 353 mm yr^{-1}) is observed for the southernmost catchment, and the maximum (i.e., 1288 mm yr^{-1}) in a northern catchment. The mean maximum monthly precipitation oscillates between 99 and 387 mm $month^{-1}$, and is strongly related to the mean annual precipitation (see Table 4). The discharge (Q_{90}) shows large variability, with a maximum value of 312 m^3 s^{-1} in the central western Andes. There is a strong positive correlation (Spearman's r > 0.9) between the discharge and the catchment area (Table 4). The lithological erodibility index varies between 0.39 and 0.99 and is lowest in the northernmost catchments dominated by sedimentary rocks (see S3).

Along the latitudinal gradient, there is a systematic variation in land cover with a dominance (> 85 % of total surface area) of savannas and forests in the southern catchments (11° – 14.5° S). In the central area (6° – 11° S), the areal coverage of grasslands systematically increases (and savanna decreases) from south to north between 9° and 11° S, with about 60 % grasslands and 35 % savanna at 9°S. Between 6°and 9° S, grasslands remain the dominant land cover having > 70 % areal coverage. In this part, the highest percentages of (irrigated) croplands can be found. The northern area (3° – 6° S) is mainly covered by grasslands (> 70 %). Over the period 2012–2018, an increase in vegetation cover was observed in the central area and at # 1 station (Conta) with a maximum vegetation increment of about 12 % in the # 12 (Yonan) and # 13 (Raca Rumi) catchments. In six catchments in the northern part, a reduction of vegetation cover is observed, up to 19 % for the #21 catchment in Zarumilla basin. The land cover is strongly associated to the precipitation patterns, with a strong positive relation between the mean annual precipitation (AvgP) and the percentage of land covered by forest and savanna (Spearman's r = 0.68, Table 4). Catchments with dominance of forest and savanna vegetation are typically located in the northern part of the study region where the mean annual precipitation is above 1000 mm yr^{-1}; Fig. 5). A negative correlation exists between precipitation and the surface area covered by grasslands and shrublands (Spearman's r = -0.93, S4).

4.2.2. *Correlation between SSY and environmental factors*

Given the wide scatter of the catchment's spatial distribution, the correlation between the specific sediment yield and the environmental variables is generally weak with Spearman correlation coefficients below 0.55 (Fig. 6, and S4). Therefore, we included here the environmental variables that are marginally correlated to the specific sediment yield using a significance level of 0.90. The marginally significant variables are plotted against specific sediment yield in Fig. 7. The SSY is positively related to catchment area (r = 0.48), and topographic relief (r = 0.44). Other topographic variables such as the mean slope gradient or river steepness do not show significant correlation with the SSY. A same observation can be made for lithological strength and erodibility that are only weakly (positively) correlated to SSY. None of the precipitation variables shows strong correlation with SSY (see Fig. 6), instead all of them present a weak negative correlation. River discharge, in particular the 50 % and 90 % quartile of the discharge values, shows positive correlation with the average annual sediment load, SSY (r = 0.49 and 0.50 respectively), see Table 4. The land cover, and land cover change, data show the importance of croplands in controlling specific sediment yield, with a strong and positive relationship between the proportion of the area covered by crops and the SSY (r = 0.55).

4.2.3. *Uni- and multi-variate regression model*

First, univariate regression models were constructed based on the observational data for the 21 catchments. In the univariate models, we use a power law fit between the specific sediment yield and the three most significant physical variables, i.e., catchment area, discharge and topographic relief (Table 5). The univariate models have a coefficient of determination, R^2, of 0.34, 0.37 and 0.45 respectively, and a power law of the topographic relief can explain up to 45 % of the observed variance in SSY (Fig. 8 a-c). Second, we verified if a bi-variate model improved the model performance. When we combined discharge and steepness index (ks_{50}), the model $SSY = 0.56\ Q_{90}^{0.65}\ ks_{50}^{0.55}$ had a R^2 of 0.55 and a p-value 0.001. Because of the strong correlation between discharge and catchment (r > 0.9), we implemented a runoff variable ($Q_{90}\ A^{-1}$) to avoid collinearity in the regression analysis. The model performance of the bi-variate model ($SSY = 0.86\ (Q_{90}\ A^{-1})^{0.15}\ R^{0.85}$) slightly improved with a R^2 of 0.47 (Table 5). When plotting the modelled against the observed SSY values, we still observed an important scatter for the higher-than-average SSY values (Fig. 8 d).

For the multivariate regression model, we included anthropogenic variables in the sediment model in the form of land cover variables. The land cover variable with the highest correlation to SSY, the percentage of cropland area (%C), was first added to the model. Including the cropland area improved the overall model performance ($R^2 = 0.57$, RSE = 0.21) and the scatter in the modelled SSY was slightly reduced (Fig. 8 e). We further tested if adding additional land cover variables that were positively related to the SSY (Fig. 6) improved the model fit. When adding the variable forest and savannas (%F&Sa), the performance of our model incremented ($R^2 = 0.63$, Fig. 8f). However, the positive correlation between SSY and the percentage of forest and savannas is contrary to what is expected. Regularly, a dense vegetative cover inhibits the sediment production and transport (Molina et al., 2015; Vanacker et al., 2022).

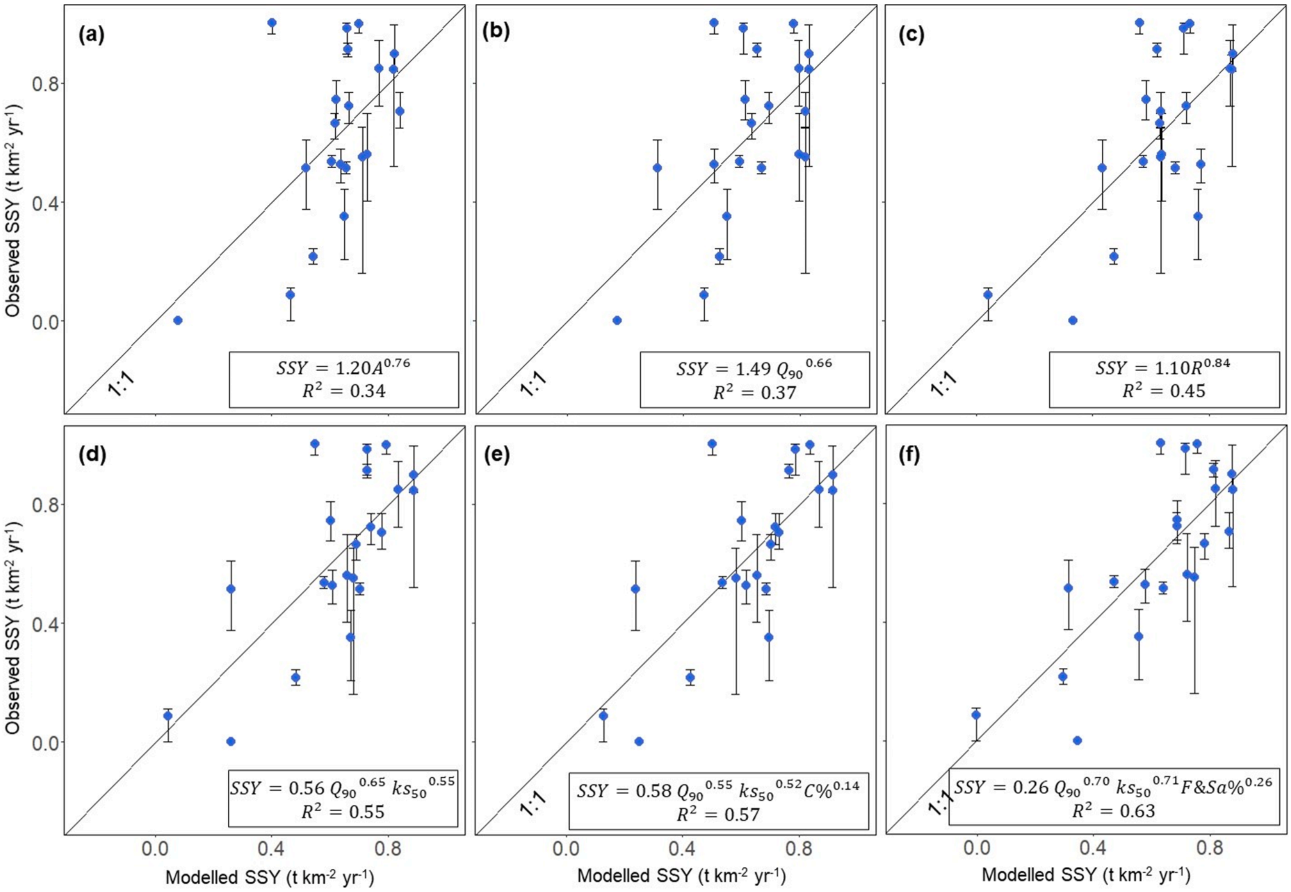

Fig. 8. Plot of the observed vs the modelled SSY. (a-c) univariate models including area discharge (Q_{90}) and relief. (d) Bi-variate model, adding the steepness index (ks_{50}). (e-f) Tri-variate models, adding the percentage of croplands (%C) and the percentage of forest and savannas (%F&Sa) to the discharge (Q_{90}) and steepness index (ks_{50}). The boxes present the regression equation, the R^2 and the residual standard error, RSE, as measures of goodness-of-fit.

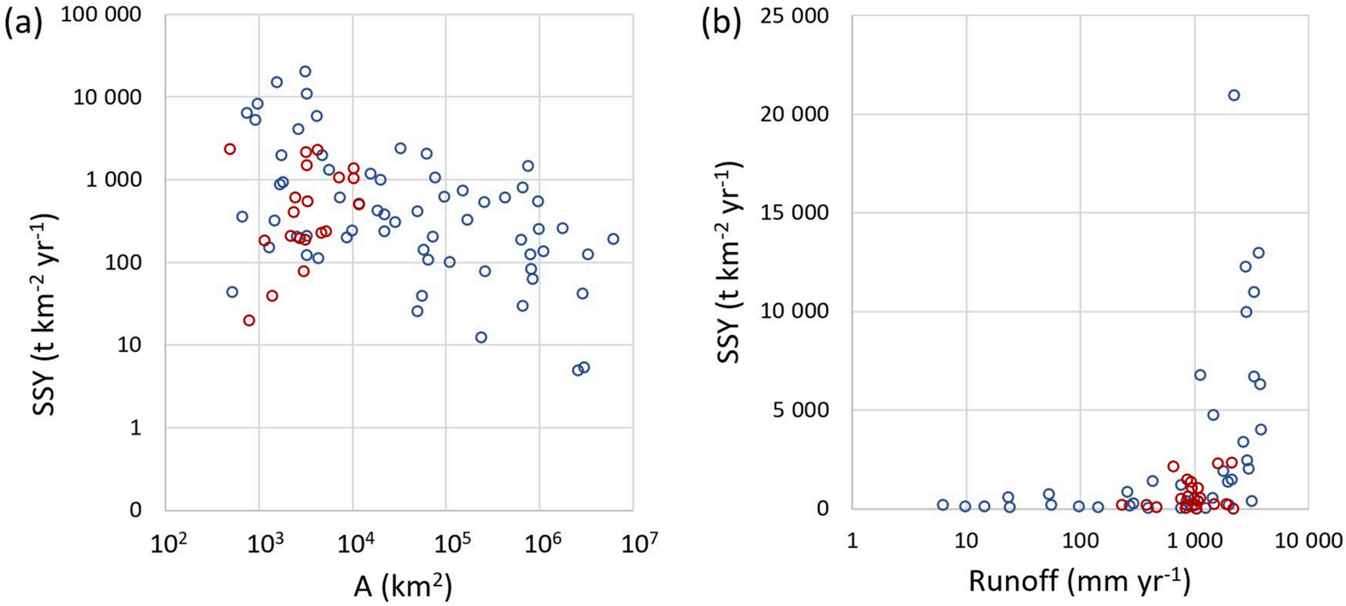

Fig. 9. A contrasting view of our data (red dots) and a global database (blue points). (a) Specific sediment yield (SSY) vs catchment area for high mountain areas (max. altitude > 3000 m). (b) SSY vs runoff for tropical and semi-tropical mountain catchments (area of < 5000 km^2). The global dataset was retrieved from Milliman & Farnsworth (2011). (For interpretation of the references to colour in this figure legend, the reader is referred to the web version of this article.)

5. Discussion

5.1. Global variation in specific sediment yield

In a global study on sediment delivery to the oceans, Milliman & Farnsworth (2011) calculated that rivers draining the South American continent deliver 530 × 106 t yr^{-1} of sediment to the Pacific Ocean. This rate is similar to the sediment delivery of rivers draining West and East Africa having sediment loads of respectively 550 × 106 t yr^{-1} and 400 × 106 t yr^{-1}. They estimated the specific sediment yield, SSY, for the rivers draining to the Pacific Ocean to range between 100 and 300 t km^{-2} yr^{-1}. The datasets that we compiled here on the Peruvian western Andes show a much wider range of specific sediment yields with several large catchments having sediment yields above 1000 t km^{-2} yr^{-1} (0.38 mm yr^{-1}) as shown in Table 2. An obvious reason for this discrepancy is the underrepresentation of time series of observational data from high relief catchments in global compilations, as well as the extrapolation techniques that tend to underestimate the temporally variable sediment yields such as the ones observed in the western Andes (Tote et al., 2011; Vanacker et al., 2020).

In Fig. 9, the observations for the Peruvian western Andes are plotted with the global data of Milliman & Farnsworth (2011). Although the new dataset only covers catchments with surface areas below 5000 km^2, its large variation in specific sediment yield can be exemplary for mountainous river catchments with a two-order-of-magnitude variation in SSY (SSY between ~ 10 t km^{-2} yr^{-1} and ~ 3000 t km^{-2} yr^{-1}, Fig. 9a). By analyzing sediment loads for nearly 500 rivers worldwide, Syvitski and Milliman (2007) concluded that catchment area and topographic relief account for about 65 % of the variance. For the Peruvian western Andes, we observed similar patterns where catchment area and topographic relief are positively related to specific sediment yield, and can explain up to 39 % of the observed variance (Table 5). The empirical sediment yield model reveals the importance of runoff as a predictor of specific sediment yield. The hydrological control on sediment yield is confirmed when plotting our data with the global database (Fig. 9b). Data from regions with strong environmental gradients such as the Peruvian western Andes can allow to further unravel the nonlinear relation that exists between specific sediment yield and runoff (mm yr^{-1}).

5.2. Regional variation in specific sediment yield

The specific sediment yield varies strongly along the Peruvian western Andes (Fig. 4). In our dataset, the southern part (11° – 14.5° S) shows systematically low and uniform yields of 39 to 551 t km^{-2} yr^{-1} (0.02–0.21 mm yr^{-1}) (Table 3). These values are within the range of published specific sediment yields in Chile, where Pepin et al. (2010) and Carretier et al. (2013) reported values below 700 t km^{-2} yr^{-1} (0.26 mm yr^{-1}). The central part (6° - 11° S) is characterised by systematically higher-than-average SSY of 2130 to 2300 t km^{-2} yr^{-1} (0.80 to 0.87 mm yr^{-1}) for the Santa River catchment (#9 and 11, Fig. 4). Anthropogenic activities such as mining were cited to have enhanced sediment production (Morera et al., 2013), although national reports (Proyecto Especial Chavimochic, 2013) rather point to the highly erodible lithology of the central part. In the northern part (3° – 6° S), the local variation in specific sediment yield is remarkable with SSY varying widely from 12 to 2 330 t km^{-2} yr^{-1} (0.01 – 0.50 mm yr^{-1}). These values fall within the range of the specific sediment yields reported for the northern Andes (Restrepo et al., 2009; Vanacker et al., 2015), where specific sediment yields of 900 to 1150 t km^{-2} yr^{-1} (0.34 – 0.43 mm yr^{-1}) are reported for rivers draining the western flank of the Colombian Andes. Similar strong variation in SSY was observed in southern Ecuador with values ranging between 16 t km^{-2} yr^{-1} (0.01 mm yr^{-1}) and > 15 000 t km^{-2} yr^{-1} (>5.66 mm yr^{-1}) for small degraded catchments (Molina et al., 2008; Vanacker et al., 2007).

However, the reported differences in sediment yield might be the result of bias in the observational data. In this study, the dataset on specific sediment yield includes information from sediment gauging stations and bathymetric studies. For the Chira-Catamayo basin where both types of data are available, we typically observed that the bathymetric studies revealed higher specific sediment yields. This might be related to fact that human made reservoirs trap a considerable fraction of sediment during extreme events, while such events are often undersampled in gauging stations; and to the fact that they account for bedload transported material. This further emphasizes the need to monitor sediment production and transport during extreme events, using alternative monitoring techniques like small reservoirs or check dams in the river channel (de Vente et al., 2013; Molina et al., 2008; Rosas et al., 2020; Verstraeten and Poesen, 2002), or non-invasive techniques such as UAV-SfM (Clapuyt et al., 2019; Eltner et al., 2016).

5.3. Regional factors controlling sediment yield

Based on the dataset of 21 catchments in the Peruvian western Andes and the resulting univariate and multivariate regression models, the catchment area, topographic relief, and river discharge were identified as the main factors explaining the variation in specific sediment yield (Fig. 7a-d). This is congruent with previous work on Andean rivers that reported how topography and runoff exert strong control on the specific sediment yield in Colombia (Restrepo et al., 2009), Chile (Pepin et al., 2010) and Ecuador (Vanacker et al., 2015; Campforts et al., 2020). Although the catchment area is often reported as an important factor, the relation between specific sediment yield and drainage area is not straightforward. Our dataset shows a systematic increase of SSY with increasing drainage area (Fig. 7) congruent with earlier observations by Restrepo et al. (2009) and Vanacker et al. (2015). Other studies on Andean rivers (e.g., Molina et al., 2008; Pepin et al., 2010) reported a decrease of SSY with catchment area. The exact form of the relationship between SSY and drainage area might depend on the geomorphic context, and more precisely sediment transport and delivery at the drainage basin scale (de Vente et al., 2007). In fluvial systems where the sediment transport capacity exceeds, or equals, the sediment delivery to the river channel, a positive relation between SSY and drainage area can be expected. This is the case for the Peruvian western Andes, where the rivers are draining the steep western escarpment of the Andean range.

The climatic control on specific sediment yield as shown by Dadson et al. (2003) and Pepin et al. (2013) was not directly confirmed in this study, as none of the precipitation variables showed positive correlation with SSY. When analyzing all 21 catchments, we even observed a negative correlation between SSY and the accumulated precipitation during the 5 % rainiest days (P_{99}, Fig. 7f). Although such results might seem to contradict previous findings at first sight, we attribute the lack of significant correlation between sediment yield and climatic variables at the regional scale rather to (i) incomplete datasets on specific sediment yields especially for stream gauge derived yields and (ii) spurious correlation of climatic with other environmental variables such as hillslope and river steepness (Table S4). The fact that there exists, for many catchments, systematic temporal variability in sediment load in response to climate variability supports this statement.

Our results illustrate the difficulty of deriving sediment yields from stream-gauged data in montane catchments that are prone to extreme weather events. The derivation of reliable sediment yields strongly hinges on the assumption of stationarity in the discharge records, and the reliability of the sediment rating curve for extreme events (Vanacker et al., 2020). In this study, the sediment rating curves showed a low performance (catchments #14, 16, 17 and 18), even with an elevated number of samples (as in #14 and 16), as very high suspended sediment concentrations (above 20 g l^{-1}) are also reported for specific events having low discharge. Besides the uncertainty on the sediment rating curve, sediment sampling was resumed during ENSO events. The lack of correlation between the specific sediment yield and the climatic variables might be an artifact of the incomplete datasets for stream gauge-derived sediment yields. When comparing the specific sediment yield estimates that are based on the sediment rating curve (such as #14 and #16) and the ones based on bathymetric data (#15), we observed clear discrepancies whereby the latter are two to three times higher than the former SSY values. The apparent underestimation of the specific sediment yield from sediment gauging points to the difficulty of extrapolating flow frequency and sediment rating data in non-stationary hydrological regimes characterized by extreme events, an issue that was raised before by Vanacker et al. (2020) for the Tropical Andes. By comparing catchment-average erosion rates from sediment rating curves, landslide inventories and cosmogenic radionuclides, they showed that sediment gauging-based average sediment yields were roughly one order of magnitude lower than landslide-related sediment fluxes and the cosmogenic radionuclide-derived erosion rates.

Lithological erodibility shows a weak (positive) correlation (~0.30) with specific sediment yield. The influence of lithology on regional patterns of sediment yield is not yet clear. Several studies in the Andes reported strong lithological control on erosion and river incision (e.g., Campforts et al., 2020; Carretier et al., 2013) while the other studies did not consider lithology as an important factor. At a continental scale, lithology and rock strength is often considered to play a secondary role in the explanation of specific sediment yields (Syvitski and Milliman, 2007; Milliman and Farnsworth, 2011). We suggest that further research is needed to identify the role of lithology on sediment production and transport.

Land cover variables are significantly associated to specific sediment yield. The percentage of cropland in the upstream catchment is the variable that has the strongest correlation with the SSY (Fig. 7): catchments with few croplands have systematically the lowest SSY, and the SSY increases rapidly even with small increments of cropland area of 3 to 4 % (Fig. 7e). Although the areas covered by croplands remain small, their location in the river valleys and close to the river network probably plays a major role in the transfer of eroded material to the river network during rain events. Likewise, previous studies have identified population density, livestock density, road infrastructure, and mining activities as important anthropogenic triggers of sediment production (Morera et al., 2013; Balthazar et al., 2013; Restrepo et al., 2015).

However, the exact role of land cover in protecting or enhancing sediment yield is difficult to assess at a regional scale because of spurious correlation between land cover, topography (topographic relief and channel steepness) and river discharge. Likewise, in some cases the correlation between vegetative cover and SY is contrary to previous studies in the matter (Molina et al., 2008; Restrepo et al., 2015). Expanding the dataset with new observational data would help to elucidate the additional effect of land cover on sediment yield. There is a particular lack of knowledge on sediment fluxes during extreme but infrequent rainfall events, and new monitoring techniques using e.g. in-situ backscatter turbidity sensors or acoustic doppler meters may open new perspectives for continuous suspended sediment estimates. A larger empirical dataset on sediment yields would permit a detailed geographic analysis whereby sediment yields can be analysed per regional environment.

6. Conclusions

Understanding the environmental factors controlling sediment yield is of paramount importance for water quality and sediment management in the Tropical Andes. Based on a literature review, we identified a clear gap in observational data on sediment yield for rivers draining the western flank of the Andes to the Pacific Ocean. We addressed this knowledge gap by compiling a coherent dataset on specific sediment yield for the Peruvian western Andes over a 30-year' period (1990 – 2019). The dataset was constructed from data of sediment gauging stations, water turbidity measurements, bathymetric surveys, and was complemented with existing information from previous studies in the region.

The specific sediment yield varies strongly along the Peruvian western Andes. Based on the information from 21 catchments, we reported (i) higher-than-average SSY values in the central part (6°-11° S) with SSY of 2130 and 2300 t km^{-2} yr^{-1}, (ii) low and uniform yields of 39 to 551 t km^{-2} yr^{-1} in the southern part ($11^\circ - 14.5^\circ$ S), and strong local variation in SSY in the northern part ($3^\circ - 6^\circ$ S) with values varying from 12 to 2330 t km^{-2} yr^{-1}. About 55 % of the observed variance can be explained by river discharge (Q_{90}) and river channel steepness (ks_{50}). By adding an anthropogenic variable based on land cover, the explained variance in SSY only increases up to 63 % because of spurious correlation between land cover, river discharge and topography. Lithology and precipitation did not show a strong correlation with SSY.

The study further calls attention to the scarcity of empirical data on sediment yield for the western Andes, and the difficulty of reconstructing sediment yields from gauging data in areas with non-stationary hydrological regimes associated to extreme ENSO events. Alternative methods for sediment yield estimates based on e.g. reservoir or lake sedimentation or continuous turbidity sensors may allow one to overcome uncertainties associated with systematic undersampling of extreme events in gauging stations.

Author contributions

VV and MR conceived the research study, MR compiled the geospatial database and data on precipitation, river discharge, and sediment yield. MR conducted the statistical analyses, with backstopping of VV. WV contributed to shaping the research and analyses. MR, VV and WV prepared a first draft of the manuscript and MR and VV prepared the final version, all the authors reviewed and approved the manuscript.

Declaration of Competing Interest

The authors declare that they have no known competing financial interests or personal relationships that could have appeared to influence the work reported in this paper.

Data availability

Data will be made available on request.

Acknowledgements

The research was supported by a PhD Scholarship to MR from the Conseil de l'Action Internationale from UCLouvain (Grant No. ADRI/CD/CA/2016-NR 51) and was supported by the Belgian Académie de recherche et d'enseignement supérieur (ARES, Belgium) as part of the POP project "Erosion and sediment yield in response to climate change and variability in Andean watersheds" awarded to VV and WV. We further acknowledge Christian Hüggel (University of Zurich), and the Glaciares+ project for feedback and continuous support. We thank the Superintendence of Services and Sanitation (SUNASS) of Peru, National water management projects Chavimochic, Chira-Piura, Jequetepeque-Zaña and Olmos-Tinajones, V&A Consulting Engineers, and Abel Rodriguez for the information shared.

Appendix A. Supplementary data

Supplementary data to this article can be found online at https://doi.org/10.1016/j.catena.2022.106699.

References

Aalto, R., Dunne, T., Guyot, J.L., 2006. Geomorphic Controls on Andean Denudation Rates. J. Geol. 114 (1), 85–99. https://doi.org/10.1086/498101.

Alfieri, L., Lorini, V., Hirpa, F.A., Harrigan, S., Zsoter, E., Prudhomme, C., Salamon, P., 2020. A global streamflow reanalysis for 1980–2018. Journal of Hydrology 6, 100049. https://doi.org/10.1016/j.hydroa.2019.100049.

Armijos, E., Crave, A., Vauchel, P., Fraizy, P., Santini, W., Moquet, J.S., Arevalo, N., Carranza, J., Guyoth, J.L., 2013. Suspended sediment dynamics in the Amazon River of Peru. Journal of South American Earth Sciences 44, 75–84. https://doi.org/10.1016/j.jsames.2012.09.002.

Asselman, N.E.M., 2000. Fitting and interpretation of sediment rating curves. Journal of Hydrology 234, 228–248. https://doi.org/10.1016/S0022-1694(00)00253-5.

Aybar, C., Lavado-Casimiro, W., Huerta, A., Fernández, C., Vega, F., Sabino, E. and Felipe-Obando, O., 2017. Uso del Producto Grillado "PISCO" de precipitación en Estudios, Investigaciones y Sistemas Operacionales de Monitoreo y Pronóstico Hidrometeorológico. Nota Técnica 001 SENAMHI-DHI-2017, Lima-Peru.

Aybar, C., Fernández, C., Huerta, A., Lavado, W., Vega, F., Felipe-Obando, O., 2020. Construction of a high-resolution gridded rainfall dataset for Peru from 1981 to the present day. Hydrological Sciences Journal 65 (5), 770–785. https://doi.org/10.1080/02626667.2019.1649411.

Balthazar, V., Vanacker, V., Girma, A., Poesen, J., Golla, S., 2013. Human impact on sediment fluxes within the Blue Nile and Atbara River basins. Geomorphology 180–181, 231–241. https://doi.org/10.1016/j.geomorph.2012.10.013.

Bischiniotis, K., van den Hurk, B., Zsoter, E., Coughlan de Perez, E., Grillakis, M., Aerts, J. C.J.H., 2019. Evaluation of a global ensemble flood prediction system in Peru. Hydrological Sciences Journal 64 (10), 1171–1189. https://doi.org/10.1080/02626667.2019.1617868.

Borrelli, P., Robinson, D.A., Fleischer, L.R., Lugato, E., Ballabio, C., Alewell, C., Meusburger, K., Modugno, S., Schütt, B., Ferro, V., Bagarello, V., Van Oost, K., Montanarella, L., Panagos, P., 2017. An assessment of the global impact of 21st century land use change on soil erosion. Nature Communications 8, 2013. https://doi.org/10.1038/s41467-017-02142-7.

Browning, T.N., Sawyer, D.E., 2021. Vulnerability to watershed erosion and coastal deposition in the tropics. Science Reports 11, 885. https://doi.org/10.1038/s41598-020-79402-y.

Campforts, B., Vanacker, V., Herman, F., Vanmaercke, M., Schwanghart, W., Tenorio, G. E., Willems, P., Govers, G., 2020. Parameterization of river incision models requires accounting for environmental heterogeneity: insights from the tropical Andes. Earth Surface Dynamics 8, 447–470. https://doi.org/10.5194/esurf-8-447-2020.

Carretier, S., Regard, V., Vassallo, R., Aguilar, G., Martinod, J., Riquelme, R., Pepin, E., Charrier, R., Hérail, G., Farías, M., Guyot, J.L., Vargas, G., Lagane, C., 2013. Slope and climate variability control of erosion in the Andes of central Chile. Geology 41 (2), 195–198. https://doi.org/10.1130/G33735.1.

Clapuyt, F., Vanacker, V., Christl, M., Van Oost, K., Schlunegger, F., 2019. Spatio-temporal dynamics of sediment transfer systems in landslide-prone Alpine catchments. Solid Earth 10, 1489–1503. https://doi.org/10.5194/se-10-1489-2019.

Crawford, G.C., 1991. Estimation of suspended-sediment rating curves and mean suspended-sediment loads. Journal of Hydrology 129, 331–348. https://doi.org/10.1016/0022-1694(91)90057-O.

Dadson, S.J., Hovius, N., Chen, H.G., Dade, W.B., Hsieh, M.L., Willet, S.D., Hu, J.C., Horng, M.J., Chen, M.C., Stark, C.P., Lague, D., Lin, J.C., 2003. Links between erosion, runoff variability and seismicity in the Taiwan orogen. Nature 426, 648–651. https://doi.org/10.1038/nature02150.

de Vente, J., Poesen, J., Arabkhedri, M., Verstraeten, G., 2007. The sediment delivery problem revisited. Progress in Physical Geography: Earth and Environment 31 (2), 155–178. https://doi.org/10.1177/0309133307076485.

de Vente, J., Poesen, J., Verstraeten, G., Govers, G., Vanmaercke, M., Van Rompaey, A., Arabkhedri, M., Boix-Fayos, C., 2013. Predicting soil erosion and sediment yield at regional scales: Where do we stand? Earth Science Reviews 127, 16–29. https://doi.org/10.1016/j.earscirev.2013.08.014.

Dottori, F., Salamon, P., Bianchi, A., Alfieri, L., Hirpa, F.A., Feyen, L., 2016. Development and evaluation of a framework for global flood hazard mapping. Advances in Water Resources 94, 87–102. https://doi.org/10.1016/j.advwatres.2016.05.002.

Ellison, C.A., Savage, B.E., and Johnson, G.D. 2014. Suspended-sediment concentrations, loads, total suspended solids, turbidity, and particle-size fractions for selected rivers in Minnesota, 2007 through 2011: U.S. Geological Survey Scientific Investigations Report. 2013–5205, 43 p., https://doi.org/10.3133/sir20135205.

Eltner, A., Kaiser, A., Castillo, C., Rock, G., Neugirg, F., Abellán, A., 2016. Image-based surface reconstruction in geomorphometry – merits, limits and developments. Earth Surface Dynamics 4, 359–389. https://doi.org/10.5194/esurf-4-359-2016.

ENFEN (Comisión multisectorial encargada del estudio nacional del fenómeno El Niño), 2017. Informe Técnico Extraordinario N°001-2017/ENFEN El Niño Costero 2017. Lima, July 2017.

Friedl, M. and Sulla-Menashe, D., 2019. MCD12Q1 MODIS/Terra+Aqua Land Cover Type Yearly L3 Global 500m SIN Grid V006 . NASA EOSDIS Land Processes DAAC. Accessed 2021-01-29 from 10.5067/MODIS/MCD12Q1.006.

Gardi, C., Angelini, M., Barceló, S., Comerma, J., Cruz Gaistardo, C., Encina Rojas, A., Jones, A., Krasilnikov, P., Mendonça Santos Brefin, M.L., Montanarella, L., Muñiz Ugarte, O., Schad, P., Vara Rodríguez, M.I., Vargas, R., Ravina da Silva, M. (eds), 2015. Soil Atlas of Latin America and the Caribbean, European Commission - Publications Office of the European Union, L-2995 Luxembourg, 176 pp. https://esdac.jrc.ec.europa.eu/content/soil-atlas-latin-america.

Garreaud, R., Vuille, M., Compagnucci, R., Marengo, J., 2009. Present-day South American climate. Palaeogeography, Palaeoclimatology, Palaeoecology 281, 180–195. https://doi.org/10.1016/j.palaeo.2007.10.032.

González-Moradas, M.R., Viveen, W., 2020. Evaluation of ASTER GDEM2, SRTM v. 3.0, ALOS AW3D30 and TanDEM-X DEMs for the Peruvian Andes against highly accurate GNSS ground control points and geomorphological-hydrological metrics. Remote Sensing of the Environment 237, 111509. https://doi.org/10.1016/j.rse.2019.111509.

Hansen, M.C., Potapov, P.V., Moore, R., Hancher, M., Turubanova, S.A., Tyukavina, A., Thau, D., Stehman, S.V., Goetz, S.J., Loveland, T.R., Kommareddy, A., Egorov, A., Chini, L., Justice, C.O., Townshend, J.R., 2013. High-resolution global maps of 21st-century forest cover change. Science 342 (6160), 850–853. https://doi.org/10.1126/science.1244693.

Harden, C.P., 2006. Human impacts on headwater fluvial systems in the northern and central Andes. Geomorphology 79 (3–4), 249–263. https://doi.org/10.1016/j.geomorph.2006.06.021.

Harrigan, S., Zsoter, E., Alfieri, L., Prudhomme, C., Salamon, P., Wetterhall, F., Barnard, C., Cloke, H., Pappenberger, F., 2020. GloFAS-ERA5 operational global river discharge reanalysis 1979–present. Earth System Science Data 12, 2043–2060. https://doi.org/10.5194/essd-12-2043-2020.

Harrington, S.T., Harrington, J.R., 2013. An assessment of the suspended sediment rating curve approach for load estimation on the Rivers Bandon and Owenabue, Ireland. Geomorphology 185, 27–38. https://doi.org/10.1016/j.geomorph.2012.12.002.

Hartmann, J., Moosdorf, N., 2012. The new global lithological map database GLiM: A representation of rock properties at the Earth surface. Geochemistry, Geophysics and Geosystems 13, Q12004. https://doi.org/10.1029/2012GC004370.

Heinemann, H.G., 1981. A new sediment trap efficiency curve for small reservoirs. Water Resources. Bulletin 17, 825–830.

IHO, International Hydrographic Organization, 2008. IHO Standards for hydrographic surveys, 5th edition. International Hydrographic Bureau, Monaco.

Inbar, M., Llerena, C.A., 2000. Erosion processes in High mountain agricultural terraces in Peru. Mountain Research and Development 20 (1), 72–79. https://doi.org/10.1659/0276-4741(2000)020[0072:EPIHMA]2.0.CO;2.

INDECI (Instituto Nacional de Defensa Civil), 2012. Informe de emergencia N° 335. Precipitaciones pluviales que afecta distritos de Lima – Provincias. Instituto Nacional de Defensa Civil, Lima, Perú.

INDECI (Instituto Nacional de Defensa Civil), 2017. Compendio estadístico del INDECI 2017 – Gestión REACTIVA Perú. INDECI: Dirección de Políticas, Planes y Evaluación. Lima, 2017.

INGEMMET, Instituto Geológico Minero y Metalúrgico, 2016. GEOCATMIN: Geología Nacional Millón 1000000. Perú. Retrieved from https://portal.ingemmet.gob.pe/web/guest/mapa-geologico-nacional.

James, G., Witten, D., Hastie, T., Tibshirani, R., 2013. An Introduction to Statistical Learning. With Applications in R, 1st ed. Springer, New York, NY.

Kemp, D.B., Sadler, P.M., Vanacker, V., 2020. The human impact on North American erosion, sediment transfer, and storage in a geologic context. Nature Communications 11 (1), 6012. https://doi.org/10.1038/s41467-020-19744-3.

Khaleghi, M.R., Varvani, J., 2018. Sediment Rating Curve Parameters Relationship with Watershed Characteristics in the Semiarid River Watersheds. Arabian Journal for Science and Engineering 43, 3725–3737. https://doi.org/10.1007/s13369-018-3092-7.

Kober, F., Zeilinger, G., Hippe, K., Marc, O., Lendzioch, T., Grischott, R., Christl, M., Kubik, P.W., Zola, R., 2015. Tectonic and lithological controls on denudation rates in the central Bolivian Andes. Tectonophysics 657, 230–244. https://doi.org/10.1016/j.tecto.2015.06.037.

Latrubesse, E.M., Restrepo, J.D., 2014. Sediment yield along the Andes: Continental budget, regional variations, and comparisons with other basins from orogenic mountain belts. Geomorphology 216, 225–233. https://doi.org/10.1016/j.geomorph.2014.04.007.

Lehner, B., Verdin, K., Jarvis, A., 2008. New global hydrography derived from spaceborne elevation data. Eos Transactions AGU 89 (10), 93–94. https://doi.org/10.1029/2008EO100001.

Lewis, J., 1996. Turbidity controlled suspended sediment sampling for runoff-event load estimation. Water Resources Research 32 (7), 2299–2310. https://doi.org/10.1029/96WR00991.

Litty, C., Schlunegger, F., Viveen, W., 2017. Possible threshold controls on sediment grains properties of Peruvian coastal river basins. Earth Surface Dynamics 5, 571–583. https://doi.org/10.5194/esurf-5-571-2017.

López-Tarazón, J.A., Batalla, R.J., Vericat, D., Francke, T., 2009. Suspended sediment transport in a highly erodible catchment: The River Isábena (Southern Pyrenees). Geomorphology 109 (3–4), 210–221. https://doi.org/10.1016/j.geomorph.2009.03.003.

Luque, G., Rosado, M., Pari, W., Peña, F., Huamán, M., 2020. Peligro geológico en la región Lima. INGEMMET, Boletín, Serie C: Geodinámica, 76, 298 p., 9 mapas. https://hdl.handle.net/20.500.12544/2571.

Martini, L., Faes, L., Picco, L., Iroumé, A., Lingua, E., Garbarino, M., Cavalli, M., 2020. Assessing the effect of fire severity on sediment connectivity in central Chile. Science of The Total Environment 728, 1339006. https://doi.org/10.1016/j.scitotenv.2020.139006.

Mettier, R., Schlunegger, F., Schneider, H., Rieke-Zapp, D., Schwab, M., 2009. Relationships between landscape morphology, climate and surface erosion in northern Peru at 5°S latitude. International Journal of Earth Sciences 98, 2009. https://doi.org/10.1007/s00531-008-0355-7.

Milliman, J., Farnsworth, K., 2011. River Discharge to the Coastal Ocean: A Global Synthesis. Cambridge University Press, Cambridge, UK. https://doi.org/10.1017/CBO9780511781247.

Molina, A., Govers, G., Poesen, J., Van Hemelryck, H., De Bièvre, B, Vanacker, V., 2008. Environmental factors controlling spatial variation in sediment yield in a central Andean mountain area. Geomorphology 98 (3–4), 176–186. https://doi.org/10.1016/j.geomorph.2006.12.025.

Molina, A., Vanacker, V., Mora, D., Balthazar, V., 2015. Multidecadal change in streamflow associated with anthropogenic disturbances in the tropical Andes. Hydrology and Earth System Sciences 19, 4201–4213. https://doi.org/10.5194/hess-19-4201-2015.

Moquet, J.S., Morera, S., Turcq, B., Poitrasson, F., Roddaz, M., Moreira-Turcq, P., Espinoza, J.C., Guyot, J.L., Takahashi, K., Orillo-Vigo, J., Petrik, S., Mounic, S., Sondag, F., 2020. Control of seasonal and inter-annual rainfall distribution on the

Strontium-Neodymium isotopic compositions of suspended particulate matter and implications for tracing ENSO events in the Pacific coast (Tumbes basin, Peru). Global and Planetary Change 185, 103080. https://doi.org/10.1016/j.gloplacha.2019.103080.

Morera, S.B., Condom, T., Vauchel, P., Guyot, J.L., Galvez, C., Crave, A., 2013. Pertinent spatio-temporal scale of observation to understand suspended sediment yield control factors in the Andean region. Hydrology and Earth System Science 7, 4641–4657. https://doi.org/10.5194/hessd-10-625-2013.

Morera, S.B., Condom, T., Crave, A., Steer, P., Guyot, J.L., 2017. The impact of extreme El Niño events on modern sediment transport along the western Peruvian Andes (1968–2012). Science Reports 7, 11947. https://doi.org/10.1038/s41598-017-12220-x.

Mudd, S.M., Attal, M., Milodowski, D.T., Grieve, S.W.D., Valters, D.A., 2014. A statistical framework to quantify spatial variation in channel gradients using the integral method of channel profile analysis. Journal of Geophysical Research. Earth Surface 119, 138–152. https://doi.org/10.1002/2013JF002981.

Mudd, S. M., Clubb, F. J., Gailleton, B., Hurst, M. D., Milodowski, D. T., Valters, D. A., 2018. The LSDTopoTools Chi Mapping Package (Version 1.11). Zenodo. 10.5281/zenodo.1291889.

Navratil, O., Esteves, M., Legout, C., Gratiot, N., Nemery, J., Willmore, S., Grangeon, T., 2011. Global uncertainty analysis of suspended sediment monitoring using turbidimeter in a small mountainous river catchment. Journal of Hydrology 398 (3–4), 246–259. https://doi.org/10.1016/j.jhydrol.2010.12.025.

Oñate-Valdivieso, F., Bosque Sendra, J., 2014. Semidistributed Hydrological Model with Scarce Information: Application to a Large South American Binational Basin. Journal of Hydrologic Engineering 19 (5), 1006–1014. https://doi.org/10.1061/(ASCE)HE.1943-5584.0000853.

PECH (Proyecto Especial Chavimochic), 2013. Proyecto Chavimochic, Tercera etapa, Estudio de factibilidad. Vol.4, Anexo 4: Transporte de sólidos. Proyecto Especial Chavimochic, Peru.

Pepin, E., Carretier, S., Guyot, J.L., Escobar, F., 2010. Specific suspended sediment yields of the Andean rivers of Chile and their relationship to climate, slope and vegetation. Hydrological Sciences Journal 55 (7), 1190–1205. https://doi.org/10.1080/02626667.2010.512868.

Pepin, E., Guyot, J.L., Armijos, E., Bazan, H., Fraizy, P., Moquet, J.S., Noriega, L., Lavado, W., Pombosa, R., Vauchel, P., 2013. Climatic control on eastern Andean denudation rates (Central Cordillera from Ecuador to Bolivia). Journal of South American Earth Sciences 44, 85–93. https://doi.org/10.1016/j.jsames.2012.12.010.

Poveda, G., Espinoza, J.C., Zuluaga, M.D., Solman, S.A., Garreaud, R., van Oevelen, P.J., 2020. High Impact Weather Events in the Andes. Front. Earth Sci. 8, 162. https://doi.org/10.3389/feart.2020.00162.

Rau, P., Bourrel, L., Labat, D., Melo, P., Dewitte, B., Frappart, F., Lavado, W., Felipe, O., 2017. Regionalization of rainfall over the Peruvian Pacific slope and coast. Int. J. Climatol. 37, 143–158. https://doi.org/10.1002/joc.4693.

Restrepo, J.D., Kjerfve, B., Hermelin, M., Restrepo, J.C., 2006. Factors controlling sediment yield in a major South American drainage basin: the Magdalena River, Colombia. Journal of Hydrology 316, 213–232. https://doi.org/10.1016/j.jhydrol.2005.05.002.

Restrepo, J.D., López, S.A., 2008. Morphodynamics of the Pacific and Caribbean deltas of Colombia, South America. Journal of South American Earth Sciences 25, 1–21. https://doi.org/10.1016/j.jsames.2007.09.002.

Restrepo, J.D., López, S.A., Restrepo, J.C., 2009. The effects of geomorphic controls on sediment yield in the Andean rivers of Colombia. Latin American Journal of Sedimentology and Basin Analysis 16 (2), 79–92. https://lajsba.sedimentologia.org.ar/index.php/lajsba/article/view/107.

Restrepo, J.D., Kettner, A.J., Brakenridge, G.R., 2020. Monitoring water discharge and floodplain connectivity for the northern Andes utilizing satellite data: A tool for river planning and science-based decision-making. Journal of Hydrology 586, 124887. https://doi.org/10.1016/j.jhydrol.2020.124887.

Restrepo, J.D., Kettner, A.J., Syvitski, J.P.M., 2015. Recent deforestation causes rapid increase in river sediment load in the Colombian Andes. Anthropocene 10, 13–28. https://doi.org/10.1016/j.ancene.2015.09.001.

Romero, C.C., Baigorria, G.A., Stroosnijder, L., 2007. Changes of erosive rainfall for El Niño and La Niña years in the northern Andean highlands of Peru. Climatic Change 85 (3–4), 343–356. https://doi.org/10.1007/s10584-007-9301-0.

Rosas, M.A., Vanacker, V., Viveen, W., Gutierrez, R.R., Huggel, C., 2020. The potential impact of climate variability on siltation of Andean reservoirs. Journal of Hydrology 581, 124396. https://doi.org/10.1016/j.jhydrol.2019.124396.

Shahgedanova, M., Alder, C., Gebrekirstos, A., Grau, H.R., Huggel, C., Marchant, R., Pepin, N., Vanacker, V., Viviroli, D., Vuille, M., 2021. Mountain Observatories: Status and Prospects for Enhancing and Connecting a Global Community. Mountain Research and Development 41 (2), A1–A15. https://doi.org/10.1659/MRD-JOURNAL-D-20-00054.1.

Syvitski, J.P.M., Milliman, J.D., 2007. Geology, Geography, and Humans Battle for Dominance over the Delivery of Fluvial Sediment to the Coastal Ocean. The Journal of Geology 15 (1), 1–19. https://doi.org/10.1086/509246.

Syvitski, J.P.M., Vörösmarty, C.J., Kettner, A.J., Green, P., 2005. Impact of Humans on the Flux of Terrestrial Sediment to the Global. Science 308, 376–380. https://doi.org/10.1126/science.1109454.

Syvitski, J.P.M., Cohen, S., Kettner, A.J., Brakenridge, G.R., 2014. How important and different are tropical rivers? - An overview. Geomorphology 227, 5–17. https://doi.org/10.1016/j.geomorph.2014.02.029.

Tenorio, G., Vanacker, V., Campforts, B., Alvarez, L., Zhiminaicela, S., Vercruysse, K., Molina, A., Govers, G., 2018. Tracking spatial variation in river load from Andean highlands to inter-Andean valleys. Geomorphology 308, 175–189. https://doi.org/10.1016/j.geomorph.2018.02.009.

Tolorza, V., Carretier, S., Andermann, C., Ortega-Culaciati, F., Pinto, L., Mardones, M., 2014. Contrasting Mountain and Piedmont Dynamics of Sediment Discharge Associated with Groundwater Storage Variation in the Biobío River. Journal of Geophysical Research: Earth Surface 119 (12), 2730–2753. https://doi.org/10.1002/2014JF003105.

Tote, C., Govers, G., Van Kerckhoven, S., Filiberto, I., Verstraeten, G., Eerens, H., 2011. Effect of ENSO events on sediment production in a large coastal basin in northern Peru. Earth Surf. Process. Landforms 36, 1776–1788. https://doi.org/10.1002/esp.2200.

Vanacker, V., Molina, A., Govers, G., Poesen, J., Deckers, J., 2007. Spatial variation of suspended sediment concentrations in a tropical Andean river system: The Paute River, southern Ecuador. Geomorphology 87 (1–2), 53–67. https://doi.org/10.1016/j.geomorph.2006.06.042.

Vanacker, V., von Blanckenburg, F., Govers, G., Molina, A., Campforts, B., Kubik, P.W., 2015. Transient river response, captured by channel steepness and its concavity. Geomorphology 228, 234–243. https://doi.org/10.1016/j.geomorph.2014.09.013.

Vanacker, V., Guns, M., Clapuyt, F., Balthazar, V., Tenorio, G., Molina, A., 2020. Distribución espacio-temporal de los deslizamientos y erosión hídrica en una cuenca Andina tropical. Pirineos 175, e051. https://doi.org/10.3989/pirineos.2020.175001.

Vanacker, V., Molina, A., Rosas, M.A., Bonnesoeur, V., Román-Dañobeytia, F., Ochoa-Tocachi, B.F., Buytaert, W., 2022. The effect of natural infrastructure on water erosion mitigation in the Andes. SOIL 8, 133–147. https://doi.org/10.5194/soil-8-133-2022.

Vauchel, P., Santinia, W., Guyot, J.L., Moquet, J.S., Martinez, J.M., Espinoza, J.C., Baby, P., Fuertes, O., Noriega, L., Puitad, O., Sondaga, F., Fraizy, P., Armijos, E., Cochonneau, G., Timouk, F., de Oliveira, E., Filizola, N., Molina, J., Ronchail, J., 2017. A reassessment of the suspended sediment load in the Madeira River basin from the Andes of Peru and Bolivia to the Amazon River in Brazil, based on 10 years of data from the HYBAM monitoring programme. Journal of Hydrology 553, 35–48. https://doi.org/10.1016/j.jhydrol.2017.07.018.

Vergara, I., Garreaud, R., Moreira, S., Araneo, D., Beigt, D., 2022. Exploring the association between landslides and fluvial suspended sediment in a semi-arid basin in central Chile. Geomorphology 402, 108129. https://doi.org/10.1016/j.geomorph.2022.108129.

Verstraeten, G., Poesen, J., 2002. Using sediment deposits in small ponds to quantify sediment yield from small catchments: possibilities and limitations. Earth Surface Processes and Landforms 27, 1425–1439. https://doi.org/10.1002/esp.439.

Wilks, D., 2019. Frequentist Statistical Inference. In: Wilks, D.S. (Ed.), Statistical Methods in the Atmospheric Sciences (4th Ed.), 4th. Elsevier, pp. 143–207.